ABSTRACT

Title of Thesis: EVOLUTION OF FERROMAGNETISM IN SELF-INTERCALATED CHROMIUM TELLURIDES

Tyler G. Romig, Master of Science, 2025

Thesis directed by: Professor Efrain E. Rodriguez
University of Maryland Department of Chemistry and Biochemistry

In this thesis chromium-tellurides were synthesized via solid state reaction and single crystals were grown via chemical vapor transport reactions. Both monoclinic and hexagonal Cr_7Te_8 phases were synthesized and magnetic susceptibility measurements and field sweeps were preformed. Arrott plots were generated to determine the exact Curie temperature of the monoclinic and hexagonal phases of 328 K and 342 K respectively. The disordered phase sample shows a unique meta-magnetic transition around 70 K. Neutron diffraction was taken on the meta-stable hexagonal phase and magnetic structures were solved showing a simple ferromagnetic arrangement at room temperature followed by a change in easy axis at 150 K, and finally a spin-recant to the *c*-axis at 5 K. The addition of an anti-ferromagnetic component and a magnetic propagation vector of $k = (\frac{1}{2}, \frac{1}{2}, 0)$ was also observed at 5 K. Single crystals were then grown via chemical vapor transport and macro-magnetic properties were measured utilizing a SQUID magnetometer. Several samples showed the same meta-magnetic transition around 70 K with exotic susceptibility data between in and out of plane measurements. Finally, this works next steps should include single crystal neutron diffraction of the monoclinic, trigonal, and hexagonal phase single

crystal samples to elucidate the exotic magnetic structures hinted at by the susceptibility data.

EVOLUTION OF FERROMAGNETISM IN SELF-INTERCALATED CHROMIUM TELLURIDES

by

Tyler G. Romig

Dissertation submitted to the Faculty of the Graduate School of the
University of Maryland, College Park in partial fulfillment
of the requirements for the degree of
Master of Science
2025

Advisory Committee:
Professor Efrain E. Rodriguez, Chair
Professor Efrain E. Rodriguez, Advisor
Professor Nicholas Butch
Professor Ichiro Takeuchi

Table of Contents

List of Figures

List of Tables

Chapter 1: Introduction

Two dimensional van der Waals (vdW) materials have seen a significant increase in interest among academic communities do to their potential applications in spintronics and low size weight and power devices. Graphene being the first 2D vdW material to garner attention was first discovered after the exfoliation of bulk graphite utilizing scotch tape.[3] Its monolayer of tightly packed carbon atoms in a honeycomb lattice with exceptionally high crystallinity have shown unique and unusual electronics which has led to a new paradigm of condensed-matter physics. Since the discovery of graphene and its unique monolayer physics researchers have hypothesized the combination of different vdW materials to study the chemistry and physics of the hetero structure junction and the race for discovering new vdW materials began. Materials such as Fe_3GeTe_2 were synthesized that exhibit Curie temperatures of 207 K in bulk and 130 K at the monolayer.[4] In attempts to increase the onset of ferromagnetism to around room temperature chemist began the search for ferromagnetic vdW materials by preforming doping of already known vdW materials. However, the library of 2D vdW materials continues to be limited so interest in pseudo 2D van der Waals materials has seen an increased interest in the chemistry and material science communities. In this thesis I preformed first principles research on the pseudo 2D van der Waals material Cr_xTe_y. Chromium tellurides offer a complex phase diagram with samples crystallizing in a variety of different space groups that seem to heavy influence the magnetic properties of the material.

1.1 Ferromagnets

Ferromagnets have been an important part of human technology since the turn of the century, many modern day transistors and semiconductors would be impractical without the accompanied magnetic components.[5] The search for ferromagnetic materials has led to the discovery of conducting, insulating and semiconducting ferromagnets, all of which have a variety of applications in modern technology. Ferromagnets distinguish themselves from other magnetic materials by having a large easily observable magnetic moment due to the alignment of magnetic moments of magnetic ions in the solid material. Picture below in Figure 1.1 is a simple representation of what ferromagnetic moments would look like in one dimension. Magnetic materials have recently been used to make memory banks to store information utilizing magnetic materials to store binary bits of information (0 or 1) depending on the magnetic moment orientation. An ”up” state could be representative of a 1 and a ”down” state as a 0, this has enabled modern day computers to function as we know them today.[5] However, with the emergence of solid state drives hard disk drives have become obsolete. Tuning materials Curie temperature that are pseudo 2D or 2D materials is paramount in creating devices that will be function-able at room temperature. Chromium tellurides and their vast phase diagram provide a great opportunity to utilize varying space groups and chromium amounts to tune ferromagnetic temperature to above room temperature. [2] Chromium tellurides can be synthesized to a variety of different space groups utilizing different chromium to tellurium ratios. Each crystal structure offers wildly different magnetic properties with the vast majority of them being ferromagnetic to some degree.[2, 6, 7] A recent study by Wen et al has shown Curie temperature can be tuned to higher temperatures with thinner samples. Typically reducing layer thickness of 2D van der Waals materials results in a monotonic decrease in Curie temperature.[2] Interestingly, Cr_2Te_3 shows the opposite of this widely observed property. One, two, and four

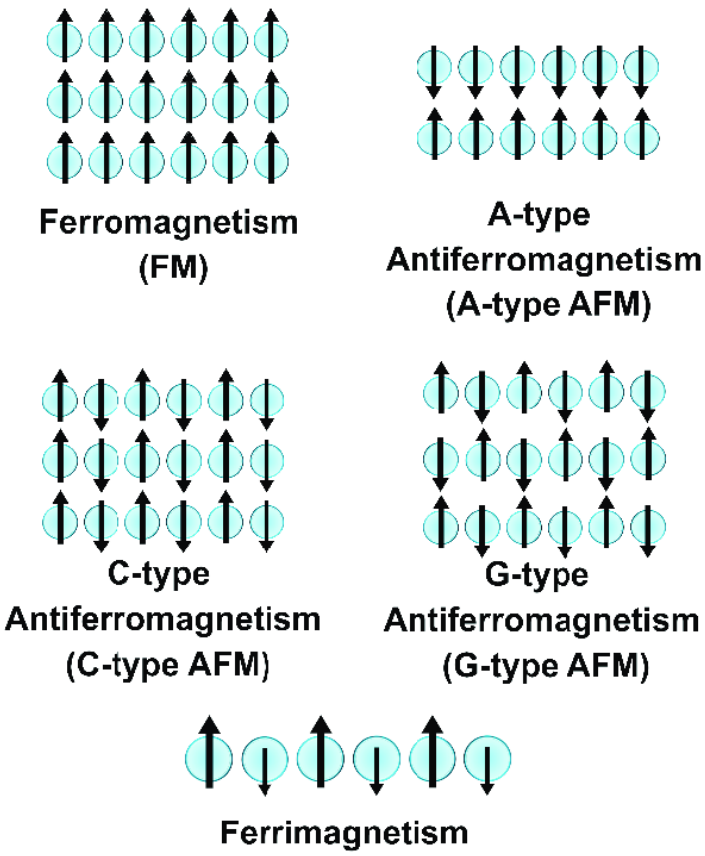

Figure 1.1: Ferromagnetism, Anti-ferromagnetism and ferrimagnetism representation. Arrows represent magnetic moment vectors.[1]

unit cell thick single crystals were grown via van der waals epitaxy on a mica substrate and an increase of Curie temperature was observed.[2] Chromium-tellurides exact magnetic mechanism for the enhancement of T_c is still unknown but Wen et al hypothesize that it may be due to the ultra-thin samples unique surface chemistry that would be similar to doping in bulk. When the chromium telluride is sufficiently thick the unique surface chemistry resembles the bulk and the doping-like effect is decreased leading to its conventional Curie temperature. With the possibility of tuning ultra-thin ferromagnetic materials to have above room temperature magnetism, the realization of new hetero-structure devices may be just upon the horizon. The discovery of 2-D van der Waals materials has raised significant interest in the scientific community due to their potential application in spintronics devices.

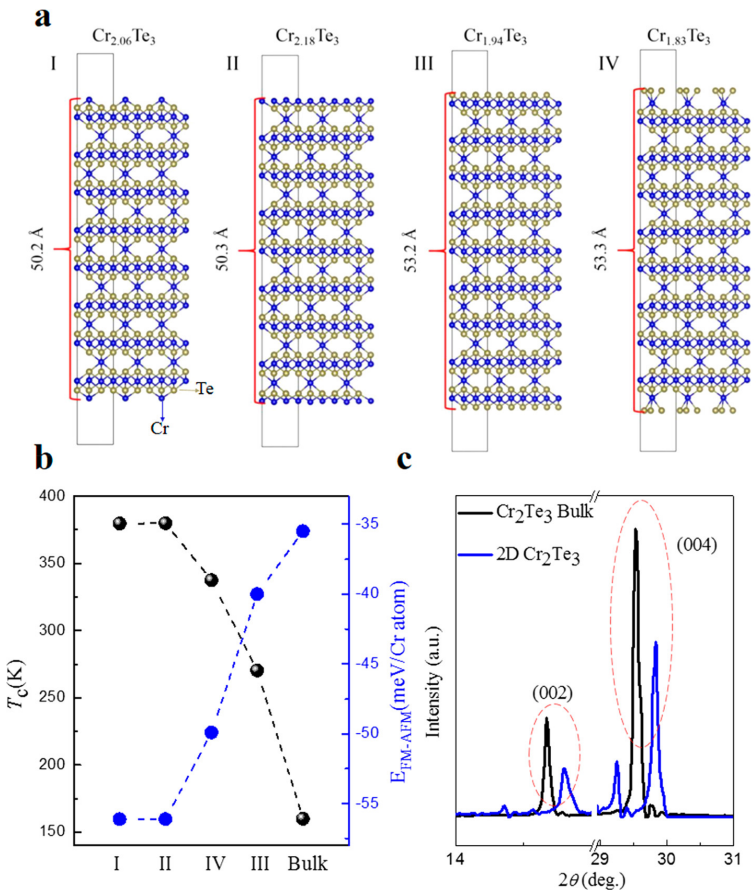

Figure 1.2: Study showing Curie temperature increase with decreasing layer thickness of Cr_2Te_3.[2]

While T_c increase is seen with thinner samples in Cr_2Te_3 the opposite is usually true leading scientists to begin the search for new 2D van der Waals materials and so called pseudo 2D vdW materials. Below two dimensional van der Waals materials and pseudo van der Waals materials will be discussed.

1.2 Two Dimensional Materials

Two dimensional van der Waal's materials have garnered significant interest recently due to their ability to form hetero-structures comprised of one atom thin layers of varying chemical make up.[8] The 2D layers typically have vastly different properties than their

three dimensional counter parts. The race to find 2D vdW ferromagnets emerged and scientists began synthesizing various transition metal dichalcogenides due to their wide electrical properties. Transition metal dichalcogenides (TMD's) consist of compounds with the broad formula MX_2 where M is any transition metal and X is a chalcogen. TMD's can form insulating or semiconducting compounds when M is Ti, Zr, W or they can form metallic and semi-metallic compounds when M is Cr, V, Nb.[8] Interesting magnetic phenomena have been observed in TMD's to include itinerant ferromagnetism in atomically thin samples as well as A-Type anti ferromagnetism in tantalum selenides.[4, 9] Research into TMD's saw the important discovery of Fe_3GeTe_2 (FGT) a two-dimensional vdW with high Curie temperatures of roughly 205 K in bulk material.[10] FGT was discovered to have intrinsic out of plane anisotropy even when exfoliated to the monolayer.[10] However, upon exfoliation the paramagnetic to ferromagnetic transition quickly dropped. While long range magnetic ordering is observed it is quickly suppressed via thermal fluctuations according to the Mermin-Wagner theory.[11] Chromium tellurides may serve as a good candidate for room temperature ferromagnetism due to the observed increase in Curie temperature upon lessening the amount of layers.[2] Gong et al discovered that these thermal fluctuations can be counter acted by magnetic anisotropy and confirmed the existence of intrinsic long range ordering via scanning magneto-optic Kerr microscopy.[11] Creating heterostructure devices relies heavily on the unique properties that will appear at the 2D interface of different layers. First principle studies by Gong et al of 12 metal-graphene interfaces was preformed and detailed electronic and atomic physiosorption and chemisorption properties were studied. [12] For chemisorption interfaces the combination of Pauli-exclusion energy shifts and hybridized states tend to lead to band gap opening. Electric field can then be used to modulate graphenes energy levels creating new electronic states for device fabrication.[12] Mixed dimensional van der Waals Heterostructures have already been developed utilizing One-dimensional MnF_4 atomic wire and two-dimensional graphene.

The electronic structure of graphene was successfully changed due to sub-lattice symmetry breaking via the inter layer interaction.[13] Building out mixed dimensional heterostructures utilizing two-dimensional vdW materials and three dimensional crystals can feasibly change electronic structures at the 2D-3D interface making for new and exciting electronic and magnetic properties. Due to the lack of room temperature 2D vdW ferromagnetic materials scientists have expanded their search to pseudo 2D vdW materials, to aid in the creation of hetero-structure devices.

1.3 Pseudo Two Dimensional Materials

Chromium tellurides have been referred to in recent literature as pseudo 2D van der Waals materials due to their resemblance to Transition metal dichalcogenides crystal srtucture.[14] Chromium tellurides crystallize forming alternating layers of chromium full and chromium deficient stacking. With low enough chromium content they begin to resemble 2D vdW materials like the above described MX_2 structures. The ability to exfoliate the materials via the scotch tape method like true 2D vdW materials is limited but some amount of exfoliation can be preformed. The crystals still show magnetic anisotropy when observed in the bulk state and studies of thin films have shown the magnetic anisotropy remains in the ultra thin domain.[15] However, a common FM to AFM transition is observed in chromium tellurides and typically takes place below 100 K. Heterostructures of chemical vapor deposition thin films have been made with near room temperature device performance. Chromium tellurides offer interesting magnetic properties for application in heterostructure devices due to their dual FM-AFM behavior.[16] In thin film grown samples magnetic skyrmions with random chirality have been observed lending to Cr_7Te_8 being an exciting candidate for device fabrication.[17] In order for usable room temperature devices to be made efforts towards synthesizing high temperature 2D magnets have been made.[18] Typical efforts

have relied on exfoliation of bulk materials on the wafer scale but often results in lower than bulk curie temperatures. Due to this pseudo 2D materials have piqued the interest of the scientific community and self intercalated TMD's have shown promise of raising low dimensionality materials operating temperatures to beyond room temperature. The promise Cr_2Te_3 shows with increasing curie temperature as thickness decrease make the chromium telluride family ideal for study.[2]

1.4 Chromium Tellurides

Chromium tellurides crystallize in a variety of different space groups, each of which offers unique magnetic structures. The typical overall structure is the Ni-As type structure with hexagonal close packing of Tellurium and Chromium ions occupying the octahedral holes. Figure 1.3 below shows a basic representation of the Ni-As type structure that the chromium telluride family of compounds crystallizes in. Notably chromium fills in alternating layers of chromium full and chromium deficient stacking which may be the cause of interesting magnetic properties observed. Most of the chromium telluride library consists of ferromagnetic materials with Curie temperatures ranging from 180 K-340 K.[19] Uniquely these ferromagnetic materials are also conducting and fall into the category of itinerant magnets. Density functional theory calculations have shown the most important interactions to be the Cr3d_{z^2} orbitals along the c-axis and the Cr3d-Te 5p covalencey.[19] Crystal structures are known for hexagonal phase $Cr_{1-x}Te$ where X is at least 1, monoclinic Cr_3Te_4, trigonal Cr_2Te_3, and both monoclinic and trigonal Cr_5Te_8. While most of these compounds have magnetic susceptibility measurements documented, few have been taken to neutron diffraction sources to determine the true magnetic structure of the material.[19] Often unique metamagnetic transitions around 70 K-100 K have been seen in the chromium telluride family but few explanations have been given for the sudden change

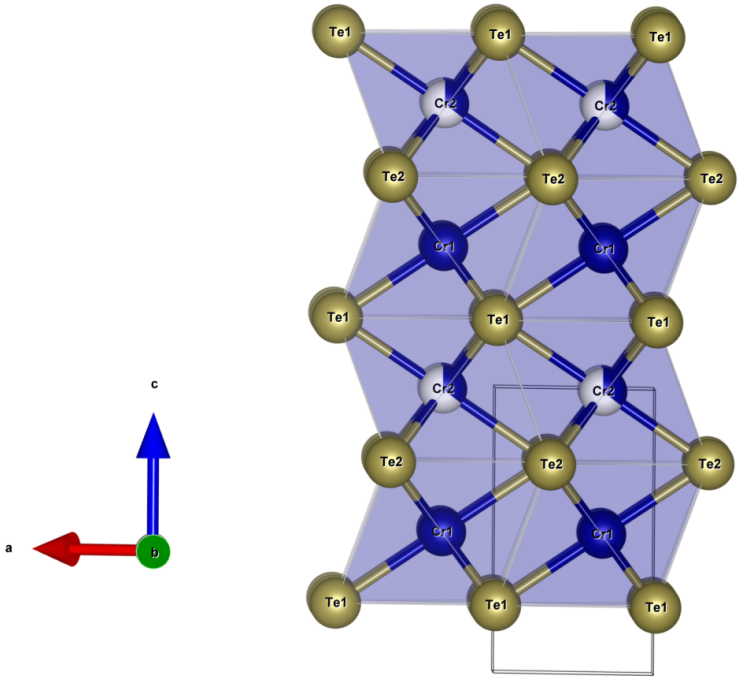

Figure 1.3: Chromium Telluride crystal structure showing chromium full and chromium deficient layers. Chromium full layers are represented by full blue spheres and chromium deficiency is represented by fractionally filled spheres.

in magnetic susceptibility.[20, 21] A neutron diffraction study of monoclinic Cr_5Te_8 shows the introduction of an antiferromagnetic phase at low temperature alongside the expected ferromagnetic phase. [21] Dzialoshinski-Moriya have derived the canted-spin structures as an inherent consequence of super exchange interactions in spin-orbit coupled systems.[21] However, this is typically a small effect and may not fully explain the AFM-like behavior observed in the chromium telluride family. Recent research has shown temperature dependent anisotropy in trigonal Cr_5Te_8. Mondal et al observe a paramagnetic to ferromagnetic transition temperature of 220 K with the addition of weak antiferromagnetic contributions below T_c.[20] Magneto-caloric effects have also been observed and were explored via field variation magnetization data near the T_c. Mondal et al's Cr_5Te_8 shows a second order mag-

netic transition of 220 K. Their critical behavior studies have suggested a quasi-2D short range type weak itinerant ferromagnetic interaction. [20, 22]

The ability to tune the Curie temperature of the Cr_5Te_8 with additional chromium content shows a monotonic increase in Curie temperature with a suppression of the AFM-like behavior observed at low temperature. Results from Zhang et al show a rapid increase in ferromagnetic transition temperature in the $Cr_{5+x}Te_8$ samples when X increases. It is hypothesized that Chromium begins to fill the inter-layer sites and causes the local spins of the intercalated Cr ions to align ferromagneticaly through the Tellurium 5d orbitals.[7] Spin-flip behavior is observed in the $Cr_5.11Te_8$ single crystals grown by Zhang et al. As seen in other Chromium telluride crystals competing anti-ferromagnetic and ferromagnetic domains are observed at low temperature. Significant splitting in magnetization versus temperature is observed and was attributed to the competition of anti-ferromagnetic and ferromagnetic domains. Zhang et al hypothesis a net ferromagnetic moment in the c-direction with competing AFM moments in the *ab* plain but no neutron diffraction study was preformed to confirm the magnetic structure of these materials.[7] Zhang et al's tunability study shows that with sufficient chromium occupancy the AFM contributions can be suppressed almost entirely where a simple ferromagnetic ordering is observed below T_c. While AFM contributions can be suppressed a spin-flip behavior is observed in samples of $Cr_{5+x}Te_8$ where x=0.11. Its observed that at low temperatures thermal energies are not enough to un-pin the magnetic domains but when sufficiently high energy temperatures are reached a sudden unpinning from the c-axis happens and magnetization increases greatly in the ab-plane before a spin-re flip is observed to the *c*-direction.

In the metal dichalcogenide $CrTe_2$ simple ferromagnetic behavior is observed with a T_c of 310 K. The $CrTe_2$ crystallizes in a trigonal structure and is meta-stable due to its decomposition recorded above 330 K.[23] Contrary to Zhang et al's work hypothesizing increasing chromium content will allow ferromagnetic domains to dominant, $CrTe_2$ shows

simple ferromagnetism and has no competing AFM behavior despite being less chromium rich than Cr_5Te_8. Magnetization versus temperature studies show a simple ferromagnetic satirization with no meta-magnetic transition recorded below T_c. Interestingly ferromagnetic moments are parallel to the ab plane which is in contrast to the Cr_5Te_8 system where the moments show its ferromagnetic easy axis to be parallel to the c-plane.[7, 23] Work preformed by Huang et al shows higher than expected chromium moments of 3.9 to 4.3μ_B which is higher than theoretically calculated values of 4.87μ_B. This phenomena is often observed in chromium dichalcogenides and is attributed to the orbital hybridization through the Cr3d-Te 5p.[24] Relatively short Cr-Cr distances are reported across layers in the c-axis. Theses short distances indicate relatively week bonding between Cr-Cr atoms. Cr_5Te_8 when doped with titanium shows differing M-Te distances depending on wether the metal is located in the full or deficient layer with the full layer having increased M-Te bonds of 2.7713 Åcompared to the deficient layers M-Te bond distances of 2.6925 Å.[24]

Cr_7Te_8 has seen increased interest due to its large Anomalous Hall Effect and its potential application in devices.[16] Polycrystalline samples has been know since 1969 where it was first reported by Hashimoto in both order (monoclinic) and disordered (hexagonal) phases.[25] Simple macro-magnetic property measurements were preformed and the addition of AFM-like moments was observed but no explanation was offered. Until recently single crystal samples had not been reported until chemical deposition methods allowed for nanosheets to be generated of hexagonal phase Cr_7Te_8. Upon AHE testing relatively high T_c nano sheets were synthesized with temperatures as large as 270K.[26] A reduction in thickness of the Cr_7Te_8 nanosheets allowed for the confirmation of ferromagnetic ordering in samples as thin as 20nm thickness.[26] The knowledge that Chromium tellurides maintain magnetism down to 20nm thickness aids in the idea of their usability in 2D/3D vdW devices.

In this research we provide a detailed neutron investigation of polycrystalline hexagonal

phase Cr_7Te_8 to better understand the micro magnetic structure of the chromium telluride family. A variety of single crystal samples have also been grown in an attempt to distinguish why meta-magnetic transitions are observed in some Cr_xTe_y samples but absent in others. As mentioned in the above chapter, an increase in chromium content in the deficient layers typically causes a decrease in the AFM contributions to the magnetic structure.[7] However, observations of meta-stable $CrTe_2$ show that even with low chromium content the AFM-like contributions can be subdued leaving a predominately ferromagnetic material. Macro-magnetic studies of varying chromium content single crystals and varying space groups may elucidate why AFM-like behavior is observed in some chromium telluride samples but not in others.

The effects of anion substitution on the chromium telluride system has also been observed via substituting telluride with S, Se and Te. Increased chromium content cause more ferromagnetic contributions but no observations on anion substitutions effect on the magnetic structure of been preformed prior to this study.[27] The addition of Selenium introduces much higher anti-ferromagnet contributions compared to its tellurium counter part. This is attributed to the shrinking of inter layer Cr-Cr distances and has already been hypothesized as the main driver for anti-ferromagnetic contributions.[27] Due to the decreased radius of the selenium ions closer Cr-chalcogen distances are observed and may also contribute to the decreased FM behavior observed in selenium substituted Cr_xTe_y.

Chapter 2: Experimental Methods

In this section I will provide the working principles of all instruments and measurement techniques as well as an explanation of the synthesis techniques used to generate the chromium tellurides being studied within this thesis. I will also introduce important concepts needed to interpret the crystal structure and magnetic properties of the studied materials.

2.1 Solid State Synthesis

Solid state synthesis is a reaction mechanism that involves taking solid starting materials, typically elemental powders, finely grinding them with a mortar and pestle or grinder and heating them to high temperatures to form a new product.[28] The reaction conditions used often require advanced knowledge of your starting compounds phase diagrams, in order for the desired phase to be formed the reaction must go to completion and mustn't stop at any kinetically favorable side product phases. Solid state synthesis reaction often depend on a plethora of variables that include shape and surface area of reactants, diffusion rates of reactants, and the thermodynamic properties of the reactants in the reaction vessel.[28] In this work solid state reactions were performed in quartz ampules that were prepared in an argon environment and purged under vacuum before being sealed via a hydrogen torch. The evacuation of atmospheric gases is important in the reaction vessel as it removes the possibility of undesirable side products like oxides forming. Another potentially harmful

result of poor vacuum in the quartz reaction vessel is the possibility of gases expanding due to the often high heats used in solid state reactions, and the quartz ampule exploding. In order for desired product to be formed the employment of starting materials as binary's or even tertiary compounds is sometimes required due to the thermodynamically favorable competing phases that may be formed. Another important factor to be aware of while preforming solid state synthesis is the cooling rate of the often molten reaction as utilizing different cooling methods can often times influence different product phases to form.[29] For example, and as we will see later in this work, the cooling of chromium tellurides slowly will result in an ordering of chromium within the unit cell and result in a lower symmetry ordered phase. Alternatively, if the reaction vessel is quenched in an ice bath a disordered phase can be secured that is higher in symmetry due to the randomly distributed nature of the vacancies. In this work high symmetry disordered phase Cr_7Te_8 is synthesized by first mixing stoichiometric amounts of chromium and tellurium, 7 to 8 parts, and grinding them to a fine powder inside of an argon filled glove box. Next, the mixed powder is sealed utilizing a hydrogen torch into an evacuated quartz ampule where it was placed in a programmable box furnaces. The disordered phase is heated to 450°C at a rate of 1 °/min and held for 12 hours. It was then heated to 1270°C at a rate of 1°/min and held for 1 hour, following this it was cooled to 1000°C where it was held for 60 hours before being quenched in an ice water bath. Powder was then removed from the quartz ampules and finely ground until a consistent texture was achieved for follow on experiments. This simple change in reaction conditions can result in wildly varying physical properties so knowledge of the cooling kinetics is a must for successful solid state reactions. Solid state reactions often result in polycrystalline samples which can then be used in combination with a vapor transport agent in a chemical vapor transport reaction to develop large bulk single crystals.

2.2 Single Crystal Growth using Chemical Vapor Transport

Often times single crystal's of product are needed for characterization due to the ability of researchers to look at unique axis's of the crystal lattice in a bulk state. In order for single crystals of non-volatile solids to be formed, a reaction mechanism called chemical vapor transport is often used. In chemical vapor transport, a volatile element is used to reversibly convert nonvolatile chemical compounds into their volatile derivatives in a sealed reactor. In this work chemical vapor transport was performed in a 13mm quartz ampule of approximately 13cm in length. The length and size of the reaction vessel can be changed to allow for varying heat gradients within the vessel which is an important variable in large crystal growth. Typically one side of the reaction vessel is held at a high temperature and the other side is places along a temperature gradient to a "cold" side. Due to the temperature gradient, the non-volatile derivative of the compound is deposited at the cold side of the reaction vessel and the transport agent is regenerated and proceed back to the hot side to form another volatile derivative.[30] This reaction is repeated and the volatile chemical vapor transport agent is regenerated and is thus a catalytic reaction mechanism. Typical chemical vapor transport agent employed are elemental iodine, aluminum chloride, and ammonium chloride. More obscure chemical vapor transport agents can be utilized if issues of side products forming are encountered. Often times chemical vapor transport reactions are done in two zone furnaces which allow for exact temperature gradients to be generated leading to increased crystal growth on the cold end of the reaction vessel. Temperature gradients and chemical vapor transport agent amounts can be varied to increase crystal size and quality when preforming chemical vapor transport reactions.

2.3 X-ray Diffraction

X-ray diffraction techniques have been used to assess the crystal structure of crystalline materials since the discovery of Bragg's law in 1912. [31] Bragg hypothesized that atoms separated by a distance d would produce constructively interfering X-ray waves in a crystal lattice due to the proximity of their sizes. Atoms in a crystal lattice are typically arranged to each other in the order of a few angstroms and the wavelength of X-rays being roughly one angstrom provides the perfect wavelength to observe constructive and destructive interference. The interference will be constructive if the difference between the different atomic planes is a multiple of 2π in 1915 Bragg was awarded the Nobel prize in physics for confirming the existence of real particles at the atomic scale due to the Bragg equation shown below in equation 2.1 below.

$$\eta\lambda = 2dsin\theta \tag{2.1}$$

The equation above relates the wavelength of X-rays (λ) with the atomic spacing between miller indices h, k, and l (d) along with the angle between incoming X-ray beam and the reflected X-ray beam (θ). In image depicting the relation ship in an atomic crystal lattice is shown below in figure 2.1. Typical lab X-ray diffractometers consist of an X-ray source,

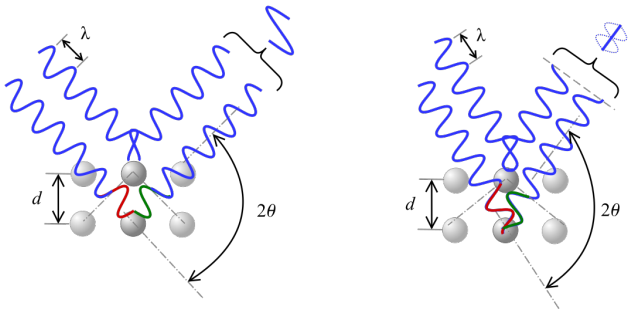

Figure 2.1: Description of Bragg's law and its relationship to X-ray diffraction techniques

a monochromator to choose the wavelength, slits to adjust the shape of the bean, a collimator to focus the X-ray beam, a sample holder, and an X-ray detector positioned at twice the sample angle (2θ).[32] X-rays have since played a critical role in determining crystal structures and their associated geometries and space groups. Below we will talk about a few of the X-ray diffraction techniques used to characterize the polycrystalline and single crystal samples generated in this work.

2.3.1 Powder X-ray Diffraction

Powder X-ray diffraction (pXRD) was employed to confirm the successful synthesis of the ferromagnetic materials investigated in this study, prior to conducting any magnetic measurements or follow-up experiments. pXRD operates on the same fundamental principles as traditional X-ray diffraction, but it differs in that the sample comprises an infinitely large number of small crystallites that are ideally randomly oriented. This random orientation simplifies the analysis, as it requires only the variation of the angle of incidence and the angle of diffraction. During the pXRD process, a diffraction pattern is generated by counting the intensity of the deflected X-ray beam as a function of these angles. Peaks in the resulting diffraction pattern will only be observable when Bragg's law is satisfied, as outlined in Equation 2.1.[33] The intensities of the diffraction peaks observed depend on a number of factors including the structure factor, the amount of materials and the absorption of the material being measured.[34] The structure factor, denoted as F_{hkl} can be mathematically described by the equation presented in Equation 2.2. In a perfect crystal, the arrangement of atoms creates a lattice that defines a reciprocal lattice. This reciprocal lattice, in turn, determines the positions and angles of the diffracted beams. The structure factor is crucial, as it dictates both the amplitude and phase of the diffracted beams. By understanding the structure factor, we gain insights into how the crystal's atomic arrangement

influences the observed diffraction pattern.[35]

$$F_{hkl} = \sum_{j=1}^{N} f_j e^{[-2\pi i(hx_j + ky_j + lz_j)]} \tag{2.2}$$

The sum is over all atoms N in the unit cell, x_j, y_j, and z_j are the positional coordinates of the ith atom and f_i is the scattering factor of the ith atom. $F - hkl$ is the vector sum of all the waves from all the units in the unit cell.[35] A typical X-ray diffraction pattern of the disordered phase Cr_7Te8 is shown below and will be discussed in much greater detail in chapter 3 of this thesis. All powder X-ray diffractions were ran on a Bruker D8 Advance

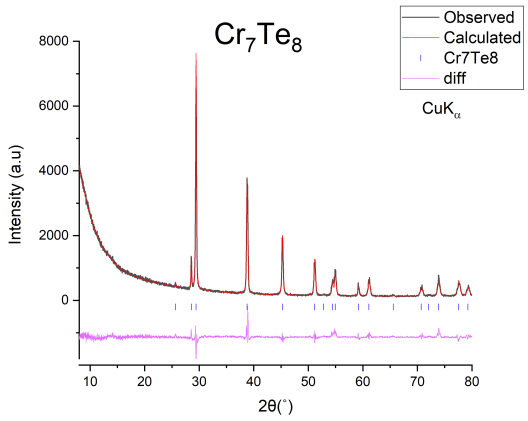

Figure 2.2: Representative powder X-ray diffraction of Cr_7Te_8 disordered phase

pictured below in figure 2.3.

2.3.2 Laue Diffraction

The Laue method of X-ray diffraction was among one of the many ways to study crystal symmetries at the turn of the 1900's. However with it being one of the more simple techniques at has taken a back seat to more complex X-ray diffraction techniques. In this thesis it was used primarily to determine the quality of grown single crystals before examining them via other means. Laue diffraction utilizes a stationary single crystal where it is

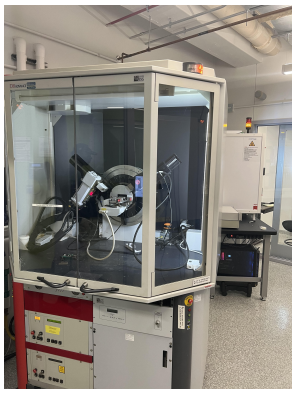

Figure 2.3: Bruker D8 Powder Diffractometer

interrogated by a stream of polychromatic X-rays and the diffracted X-rays are collected on a 2 dimensional detector.[36] Due to the polychromatic nature of the X-ray interrogation, Bragg's law is still fulfilled without the changing of incident X-ray angles like in powder X-ray diffraction explained above.[37] Laue studies can be performed on both laboratory grade X-ray detectors and higher energy synchrotron sources around the world.[37] One short coming of Laue diffraction has always been deciphering the indices of the lattice planes involved with each diffraction spot, manual methods had been used but the advancement of computer technology has quickly seen them become obsolete in favor of advanced computer programs. A representative Laue diffraction is show below in figure 2.4 and the single crystals orientation was determine for magnetic measurements. The existence of bright and sharp diffraction spots hints at the purity of the single crystal samples interrogated by Laue diffraction.

2.3.3 Synchrotron X-ray Diffraction

Synchrotron X-ray sources have become increasingly widespread which allows solid state chemists and crystallographers to explore solid structures with higher fidelity.[38] The important difference between lab X-ray diffraction and synchrotron X-ray diffraction

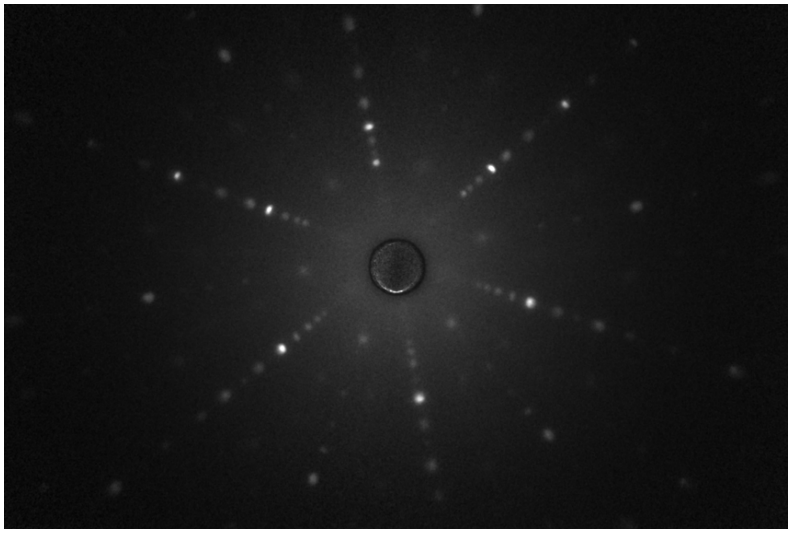

Figure 2.4: Laue diffraction of $Cr_{6.66}Te_8$ single crystal

is the X-ray generation source. In Laboratory X-rays a X-ray tube is typically used which only allows for small variations in beam parameters, due to this fact many more challenging experiments require a more intense and tunable X-ray source like Synchrotrons.[39] Synchrotron radiation sources are typically comprised of specially designed storage rings that are loaded with pre-accelerated electrons with gigaelectron volt kinetic energies, meaning they are traveling at near the speed of light.[40] Electrons are accelerated to these speeds by changing the electrons momentum via a ring of magnets, causing it to accelerate to very high speeds and reach the relativistic regime.[41, 42] Synchrotron X-ray sources also provide X-rays that are extremely intense typically 100 to 1000 times more intense than conventional laboratory X-ray tubes, the synchrotron X-rays are also highly collimated.[41] Synchrotron X-rays were used in this work to confirm the presence of multiple phases in the disordered and ordered phase chromium tellurides. Conventional laboratory X-rays were incapable of providing high enough resolution to distinguish the multiple phases instead of broad diffraction peaks. The Synchrotron source utilized in this work was the I11 Diamond Light Source.

2.3.4 Rietveld Refinement

Rietveld refinement is a technique that uses whole diffraction patterns from either neutron or X-ray sources to determine crystallographic information. The computations performed in Rietveld fitting attempt to minimize the weighted sum of the squares of the differences between the observed powder diffraction and the simulated or calculated powder diffraction patterns.[42]

$$S = \sum_i w_i (y_{obs,i} - y_{calc,i})^2 \tag{2.3}$$

The above equation shows the difference of the weighted sum of the squares of differences (s) where (w_i) is the weight value, ($y_{obs,i}$) is the observed powder diffraction data set, and ($y_{calc,i}$) is the simulated or calculated powder diffraction data set.[43] In order to obtain the calculated diffraction data set the below equation is used where B_i is the background at a point, $I(Q_i)$ is the product of intensity adjustment terms, m_{hkl} is the multiplicity of reflections hkl, O_{hkl} is the optional intensity adjustment for possible preferred orientation, Q_{hkl} is the location of reflections hkl and F_{hkl} is the structure factor term computed from Fourier transforms of the scattering unit cell.[43]

$$y_{calc,i} = B_i + I(Q_i) \sum_{hkl} m_{hkl} F_{hkl}^2 O_{hkl} P(Q_{hkl} - Q_i) \tag{2.4}$$

The units used for Q are typically the units used during the data collection process, typically angle or time of flight depending on the diffractometer utilized. Typically instrument correction terms will also need to be accounted for during the refinement process to adjust for zero offset and sometimes more complex functions need to be used to account for sample displacement factors. Due to the Rietveld refinement processing using a model to attempt to best fit the observed data, a quantification of how well fit the data is must be used. Rietveld refinement software often use a weighted-profile R factor or R_{wp} to gauge

the quality of the calculated fit to the observed data. The equation used to determine the R_{wp} is shown below in equation 2.5.

$$R_{wp} = [\sum_j w_j(y_{obs,j} - y_{calc,j})^2 / \sum_j w_j y_{obs,j}^2]^{1/2} \tag{2.5}$$

Often times the weighted profile R factor is compared to the expected R factor or R_{exp}, however this comparison is built into another statistical quantity called the reduced χ^2 shown below.[44]

$$\chi^2 = \frac{1}{j-v}\sum_j w_j(y_{obs,j} - y_{calc,j})^2 = (\frac{R_{wp}}{R_{exp}})^2 \tag{2.6}$$

In equation 2.6 above the j term is the number of observed data points and v is the number of refined parameters. Therefor, it is expected that when w_j is properly weighted χ^2 will be equal to one when no systematic errors are accounted for and will be greater than one when an imperfect model is utilized. Typically we attempt to fit our model to the best of our ability and get the χ^2 value to as close to one as possible without over fitting the data and providing a flawed model due to too many degrees of freedom.[45] In this thesis Rietveld refinements were performed on all products and sub products synthesized to determine the purity and crystallinity of the samples being studied.

2.4 Raman Spectroscopy

The Raman effect was first discovered in 1928 by the Physicist C.V. Raman, the method utilizes inelastic scattering of photons on molecular systems. [45, 46] Incident light beams interact with vibrational modes of the molecule of interest and transfer some amount of energy associated with the quantized vibrational modes. The inelastic scattering beams of interest are both stokes and anti-stokes shifted light which can be related to energy

lost or gained from the vibrational modes of the molecule of interest.[47] Each molecule provides unique vibrational modes allowing Raman to be utilized to provide a molecular fingerprint and provide insight into how molecules may change with differing connectivity and symmetry. In this thesis we attempted to utilize Raman spectroscopy as a method of deciphering how much chromium content was in the single crystals synthesized as well as see if the space group could be determined from crystal to crystal.

2.5 Energy Dispersive X-ray Spectroscopy

Energy dispersive X-ray spectroscopy was performed on the chromium telluride single crystal samples in this thesis to preliminarily confirm the compositional analysis of the single crystals grown. Energy dispersive X-ray spectroscopy or EDS/EDX is primarily coupled with electron microscopes to analyze materials at the micro and nanometer scale, however, in this thesis we were primarily interested in the chromium to tellurium ratio in the single crystal samples. EDS uses a phenomenon known as X-ray emission where an inner-shell electron is excited to a higher energy level and is replaced by a higher energy electron which is accompanied by an emission of an X-ray associated with a discreet energy level. [48] When the electron in the higher energy level replaces the lower energy electron, only transitions with allowed orbital angular momentum (l) are allowed due to the selection rules. The emission process of $K\alpha_1$ X-rays are characteristic of the transition from the outer shell to the 1st inner shell(K). While X-ray emissions can be observed from other transitions (M-L, M-K), the characteristic nature of transitions from the L shell to the K shell can be matched to specific elements allowing for compositional analysis of materials at specific locations. The energy of the X-ray emission corresponds to specific elements and the content of the element in the compound can be identified via integrating the intensity of the peak.[49] It should be noted that with lighter elements it is possible to emit an Auger

electron instead of the characteristic X-ray so EDS is generally more useful in identifying heavier elements. For the purpose of this thesis primarily focusing on chromium tellurides it was assumed EDS would give an accurate compositional makeup of the single crystal samples. While EDS analysis is a useful tool certain limitations were encountered with the

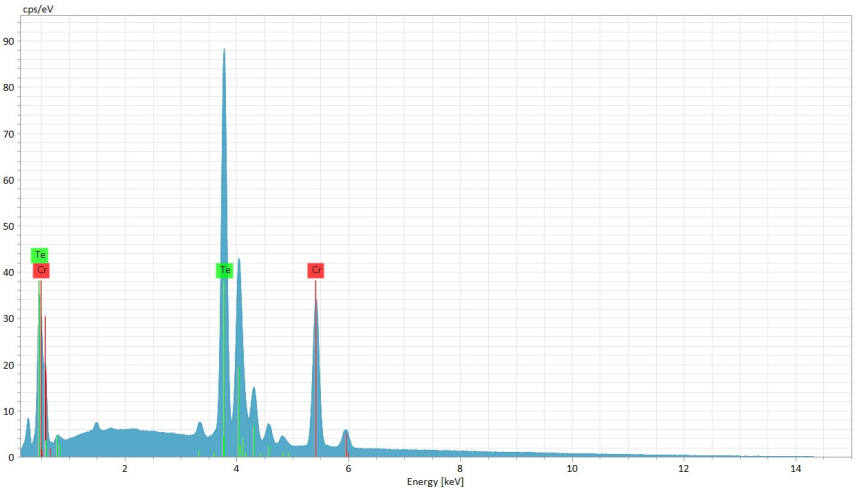

Figure 2.5: Representative EDS analysis of single Crystals of Cr_7Te_8
. The peak location x-axis (eV) determines the element of interest an the integrated intensity determines the compositional analysis of the compound.

single crystal samples which will be discussed in greater detail below in the results chapter. A representative EDS spectrum is pictured below in figure 2.5, multiple single crystals were tested and greater fidelity of each measurement will be provided in chapter 3 of this thesis.

2.6 Neutron Diffraction

Neutrons were originally discovered in 1932 by sir James Chadwick, though their existence was predicted for more than 12 years previous to that by Ernest Rutherford.[50, 51] While Neutrons are uncharged they can carry a magnetic moment which makes them suitable for determining the magnetic structure of a material. Alongside their magnetic moment

they interact directly with the nucleus of our sample material making them ideal for studying materials of low atomic weight. Due to this same factor scattering occurs differently from isotope to isotope, instead of linearly with increasing Z like in electron diffraction mentioned previously.[51, 52] While regular neutron scattering depends heavily on the nuclei of the sample, magnetic neutron scattering depends heavily on the unpaired electron cloud of the atoms being studied and can identify local magnetic structure of compounds of interest.[53] A key aspect of neutron scattering is its relatively weak interactions with materials aiding in probing the entire bulk material instead of just the surface, as would happen with much stronger interactions. The downside of this same interaction is the need for more material than would be required for electron scattering due to the stronger scattering interaction observed in the latter case. While Neutron scattering is similar to electron scattering a key difference is the addition of an associated mass with neutron diffraction of $m = 1.67X10^{-27}kg$. A neutrons wavelength is then calculated by the De Broglie wavelength equation below.[54]

$$\lambda = h/mv \tag{2.7}$$

Due to this and its associated mass it gives a de Broglie wavelength comparable to interatomic distances of 1-3 Å making it ideal for studying materials and their associated magnetic structures.[51, 54]

$$\langle \mathbf{k}_f | V(\mathbf{r}) | \mathbf{k}_i \rangle = \frac{m}{2\pi\hbar^2} \int \langle \mathbf{k}_f | V(\mathbf{r}) | \mathbf{k}_i \rangle \, d^3r \tag{2.8}$$

The equation above represents the matrix element $\langle \mathbf{k}_f | V(\mathbf{r}) | \mathbf{k}_i \rangle$, which describes the interaction between initial and final states of a quantum system under the potential $V(\mathbf{r})$, expressed in terms of the particle's mass m, the reduced Planck constant $\hbar$, and an integral over spatial coordinates.[51, 54] when $k_i = K_f$ and accounting for the very short nucleon-

nucleon interaction the equation then becomes equation 2.9 below. R explains the position of a nucleus, b_i is the scattering length.

$$V_N(r) = 2\frac{\hbar^2}{m} b_i \cdot (r - R) \tag{2.9}$$

We can now see the scattering length is different for each atom and each atoms differing isotopes. When temperatures are high enough for nuclear polarization to be limited this dependency can be left out of the equation and the final coherent scattering cross section can be described as the below equation.[51]

$$\frac{d\sigma N}{d\Omega} = |\hat{\mathbf{b}}|^2 \tag{2.10}$$

The average of the isotope population is taken over the natural element and defined as the average nucleus.[51, 55] In order to obey Bragg's law and allow for constructive interference a transfer of the neutrons momentum to the sample of interest must satisfy the reciprocal lattice space of a reflection d. Because of Neutron scatterings weak interactions with materials, high angle magnetic scattering is highly degraded and much of the prominent magnetic information will be found at low 2θ angles.

2.6.1 BT-1 Neutron Diffraction

In this thesis the BT-1 powder neutron diffractometer was utilized to observe nuclear and magnetic scattering of the disordered phase chromium telluride system. BT-1 allows for high resolution powder neutron diffraction that can be analyzed via the above mentioned Rietveld analysis. The BT-1 Instrument is a 32 detector instrument that can be used with three different monochromators to allow for interrogation of a sample with three different neutron wavelengths. In this thesis wavelengths of 2.0785 Å due to the use of the Ge(311)

monochromator which allows for the highest neutron intensity at low scattering angles.[56] Scans of the powder Cr_7Te_8 were taken at 400K, 298K (RT), 150K, and 5K.

2.6.2 Commensurate Magnetic Structures

Simple magnetic structures can be described with a propagation vector of k=0,0,0, signifying the magnetic structure has no periodic repetition across multiple unit cells.[57] For example a simple ferromagnet can be described utilizing no change of unit cell lengths in any direction. More complex magnetic structure may often require an addition of a vector to describe the magnetic structure. Utilizing K=0,0,1/2 would signify that the magnetic unit cell would be properly described by a doubling of the crystallographic unit cell in the c direction. Often times magnetic unit cells can be solved by the addition of one single k-vector but it is also possible that it requires multiple k-vectors to describe resulting in doubling, quadrupling or even greater multiplications of the crystallographic unit cell to describe.[57] The magnetic structures solved in this report were all able to be described by simple commensurate k-vectors. Commensurate k-vectors can be described as simple multiples of the nuclear unit cell and include a vast majority of magnetic structures including simple ferromagnets, antiferromagnets and ferrimagnets.[57] Translation of magnetic structures are described by the below equation.

$$\mathbf{m}_j = \sum_k \Psi_j^k e^{-2\pi i \mathbf{k}\cdot\mathbf{t}} \tag{2.11}$$

This details the periodic reputation of a magnetic unit cell similar to how nuclear structures are described by translations of nuclear unit cells.[57]

2.7 Magnetic Susceptibility

In this thesis magnetic susceptibility data was taken on both a SQUID and vibrating sample magnetometer (VSM). The magnetic transition temperatures of the single crystal chromium tellurides were often outside of the bounds of the SQUID's temperature range (1.8K-315K) so two systems were utilized in order to develop a whole picture of the unique magnetic transitions of the samples. In this section we will describe the underlying principals of magnetic susceptibility measurements as well as provide a short description of the devices utilized for the bulk of our magnetic measurements. Magnetic materials are widely studied in the fields of material science, physics and chemistry due to their important applications in modern technologies. In order to understand the experiments utilized to measure these systems a basic understanding of magnetism must first be developed. particularly the most important concept looked at in this thesis with the chromium telluride single crystals in magnetic susceptibility.

$$M = \chi H \tag{2.12}$$

The above equation represents magnetic susceptibility where M is the materials magnetization, H is the applied field by the measurement device and χ is the relationship of the materials interaction with the applied magnetic field of the measurement device (VSM or SQUID).[58] In general magnetic susceptibility tells you how your material responds to a magnetic field which helps you understand the magnetic identity of a specific sample of interest. These measurements are typically paired with temperature changes so that a change in magnetic moment can be seen at varying temperatures. Specifically with chromium t tellurides in this thesis it was typically to observe a ferromagnetic to paramagnetic transition at temperatures of 300K plus with unique metamagnetic transitions at lower temperatures around 100K. These transitions will be discussed with more fidelity in t he results and dis-

cussion chapter of this thesis. Another important concept that must be understood is the difference between field cooled (FC) and zero-field cooled (ZFC) measurements. Field cooled measurements are taken when the sample of interest is cooled in the presence of a magnetic field and zero field cooled are taken when there is zero field upon cooling of the sample.[58] Often times a divergence of these two curves is seen which is indicative of some sort of magnetic hysteresis. This in simple terms is described as a magnetic memory due to some applied field upon cooling. Exchange interactions are often the cause of this which can be described as the quantum mechanical interactions of nearby magnetic ions and how they interact with each other.[58] Often times these interactions occur directly via interaction of magnetic ion orbitals with other magnetic ion orbital but it is also possible to have itinerant magnetic systems where the interaction is via the conducting electrons and is known as an itinerant interaction.[59]

2.7.1 Vibrating Sample Magnetometer

Vibrating sample magnetometers (VSM) are capable of measuring a sample magnetic field and interactions with applied magnetic field at varying temperatures. VSM's can be used to measure magnetic susceptibility and MvH curves from liquid helium or liquid nitrogen temperatures and can also be used in conjunction with a furnace for above room temperature measurements. In this thesis measurements that required greater than 315k temperatures were taken on the VSM instrument in the Material science department at UMD. VSM work by measuring a voltage change induced by the change of an applied magnetic field, sample position or coil position. [60] Samples are typically vibrated perpendicular to the applied field where the vibrating sample then induces a voltage in the stationary detection coils. This voltage can than be used to deduce the magnetic properties of the sample. Typical VSMs also come equipped with a set of reference coils and a small

permanent magnet that is measured simultaneously with the sample of interest. Since both the sample and the reference are vibrated simultaneously the resulting voltages are directly related. [60] The known portion of the voltage can than be related to the unknown voltage of the sample and the exact magnetic moment of the sample can be backed out.[61] Exact magnetic properties with limited error are measured utilizing VSMs and in this thesis specifically the Chromium telluride systems were measured which are all ferromagnetic in nature with canting or AFM like contributions at lower temperatures.

2.7.2 Magnetic Property Measuring System (SQUID)

In this thesis a Superconducting Quantum Interference Device or SQUID was utilized to take magnetic measurements from 315K-1.8K for the chromium telluride compounds synthesized. SQUIDs utilize very sensitive detectors of magnetic flux by combining flux quantization and Josephson tunneling.[62] Josephson tunneling involves the coherent tunneling of Cooper pairs through a thin barrier separated by two superconductors. In general two kinds of SQUIDs are utilized, the first being the dc SQUID which consists of two Josephson junctions connected in parallel on a superconducting loop. They are then utilized in the voltage state with a current bias applied. When the flux loop is increased the voltage oscillates with a unique period and small changes in that voltage can be recorded and extremely small changes in flux can be observed.[62] The second kind of SQUID used in modern science is the RF SQUID which consists of a single Josephson junction inserted into a superconducting loop.[62] the amplitude of the oscillating voltage across the resonant circuit is periodic when the flux is applied. This again allows scientists to detect small changes in flux on the order of 10^{-5} Φ_0. The majority of SQUIDs utilize superconducting niobium and operate below the boiling point of liquid helium allowing for magnetic properties to be measured at near 1.8K.

Figure 2.6: Superconducting quantum interference device used for magnetometry measurements of single crystal chromium telluride samples.

2.7.3 Ferromagnetism

The materials synthesized in this thesis all show room temperature ferromagnetism with pronounced anisotropy in the c direction. A ferromagnet is a material where the atomic spins interact with each other and all try to align the others in its own direction. The net magnetic moment observed from ferromagnetic materials ends up with a pronounced alignment in one single direction.[63] In ferromagnetic materials magnetic moments of individual atoms interact with each other strongly which creates a degree of order without the presence of a magnetic field. The interactions between them originate from the quantum mechanical proprieties of spins and the so called exchange interactions which can be expressed as an energy between spins S_i and S_j which is proportional to $S_i \cdot S_j$.[63] When we include an energy for an interaction with an applied field H, the total energy of the system

can be described as seen in the equation below.

$$E = -\sum_{i,j}{}' J_{ij}\mathbf{S}_i \cdot \mathbf{S}_j - \sum_i g\mu_B \mathbf{S}_i \cdot \mathbf{H} \tag{2.13}$$

The first summation indicated that the case of the spins interaction with themselves is excluded, otherwise it is assumed that all summations extend over the entire case of the solid. The J_{ij} is called the exchange integral and in the case of a ferromagnet, is assumed to be positive so that parallel spins have a lower energy than anti-parallel spins. Due to the alignment of magnetic moments ferromagnets tend to align in a single direction in the presence of an external magnetic field which can be described by the Curie law shown below in equation 2.14.

$$\chi = \frac{C}{T - \theta_{\mathrm{CW}}} \tag{2.14}$$

C is defined as the curie constant, θ_{CW} is the curie temperature, and T is the absolute temperature in units of Kelvin.[58] The curie temperature is where the magnetic material becomes a paramagnet and below this temperature the magnet moments will align and typical reach a saturation point which can be observed via magnetic susceptibility measurements.[58] The Curie constant C can also be used to calculate the effective magnetic moment μ_b per ion as seen in equation 2.15 below.[58]

$$\mu_{\mathrm{eff}} = \sqrt{8C}\,\mu_B \tag{2.15}$$

This can than be compared to the theoretically calculated magnetic moment for the magnetic ion using equation 2.16 below.[58]

$$\mu_{\mathrm{cal}} = g_J\sqrt{J(J+1)}\,\mu_B \tag{2.16}$$

The calculated magnetic moment depends on its total angular momentum (J), and its g-tensor g_j. The magnitude of the Curie temperature can be taken as a correlation of the magnetic correlation between ions and positive values are indicative of s and observed negative values imply anti-ferromagnetism.

2.7.4 Anti-ferromagnetism

Some canting or anti-ferromagnetic behavior is observed with the chromium tellurides studied in this thesis so a brief description of the principals of anti-ferromagnetism is given in this section to aid in understanding of anti-ferromagnetic moment alignment. Anti-ferromagnetism occurs when the spins of nearest neighboring magnetic moments align anti-parallel and give the above Curie equation with a negative Curie temperature.[64]

$$\chi = \frac{C}{T + \theta_{\mathrm{CW}}} \tag{2.17}$$

This can also be described as two identical spin-up and spin-down arrays shifted by a simple lattice translation. AFM states can occur when the energy of the systems drops allowing stabilization in one array as spin-up and stabilization in another array to stabilize in a spin-down state. This can be viewed as a periodic static spin density wave whose wave vector is represented as shown below in equation 2.18.[64]

$$Q = \frac{2\pi}{a} \tag{2.18}$$

Anti-ferromagnetism can be seen in magnetic susceptibility measurements via a drop in magnetic moment, versus a magnetic saturation point as seen in ferromagnetic materials.

Chapter 3: Effects of Chromium Disorder on the Magnetic Properties of Polycrystalline Cr_7Te_8

Chromium Tellurides can be synthesized with small tweaks in chromium tellurium ratios as well as different temperature profiles upon solid state synthesis that result in vastly different crystal lattice structures and symmetries. This thesis will study the impact of ordered and disordered chromium occupation in Cr_7Te_8 and will also look at unique magnetic transitions found in varying chromium telluride single crystals.

3.1 Ordered and Disordered Phase Polycrystalline Cr_7Te_8

Cr_7Te_8 was first synthesized in 1969 by Dr Takasu Hashimoto in both the hexagonal and monoclinic phase via stolid state reaction.[25] Simple magnetic measurements were preformed but the group was limited by the technology at the time. With the emergence of 2D Van der Waals materials and their limited room temperature library, pseudo 2D materials like Cr_xTe_y have seen a reemergence in modern literature.[6, 20, 65] A More complete magnetic study was preformed on both monoclinic and hexagonal phase Cr_7Te_8 to include magnetic susceptibility measurements on a VSM and SQUID and Neutron diffraction of polycrystalline material. In this chapter we synthesize and and characterize monoclinic and hexagonal Cr_7Te_8 and compare and contrast magnetic transitions caused by a change in symmetry and variations in occupational ordering.

3.2 Solid State Synthesis

The polycrystalline pseudo-hexagonal phase Cr_7Te_8 was prepared using high quality Cr (Thermo-Scientific 200 mesh 99.94%) and Te (Thermo-Scientific 200 mesh 99.6%) inside an argon filled glove box in a stoichiometric ratio of 7 parts Cr to 8 parts Te, the elements were ground in a mortar and pestle until finely mixed and transferred to a quartz ampule. The solid mixture was then evacuated and sealed utilizing a hydrogen torch where it was placed inside a programmable box furnace and heated to 450°C at a rate of 1 °/min and held for 12 hours. It was then heated to 1270°C at a rate of 1°/min and held for 1 hour, following this it was cooled to 1000°C where it was held for 60 hours before being quenched in an ice water bath to isolate the disordered phase.

Polycrystalline monoclinic phase Cr_7Te_8 was synthesized in a similar manner with the exception of an additional temperature change after the 60 hours at 1000°C. The temperature was lowered from 1000°C to 400°C and held for 48 hours were it was allowed to cool to room temperature at the box furnaces natural cooling rate. The 400°C 48 hour hold allows for the arrangement of the chromium ions in an ordered nature due to the slow cool-down to room temperature compared to the fast quench from 1000°C which isolates the chromium in a disordered arrangement and results in a higher symmetry product.

3.3 Powder X-ray Diffraction of Cr_7Te_8

Powder X-ray Diffraction was measured in reflection geometry utilizing a Bruker D8 instrument with Cu K-α wavelength and a LynxEye detector. Rietveld refinement of the pXRD pattern at room temperature confirmed the lattice parameters of the hexagonal unit cell with dimensions of a = 4.0029(3) Å and c = 6.2392(2) Å.

Similarly, monoclinic Cr_7Te_8 was refined to have a unit cell of dimensions of a =

14.009(3) Å, b = 3.940(1) and c = 6.877(8) Å with a unique monoclinic axis of b and inversion center at 0,0,0. Powder diffraction patterns and Rietveld refinements of both the monoclinic and hexagonal phase are pictured below in figure 3.1 and figure 3.2. A marked

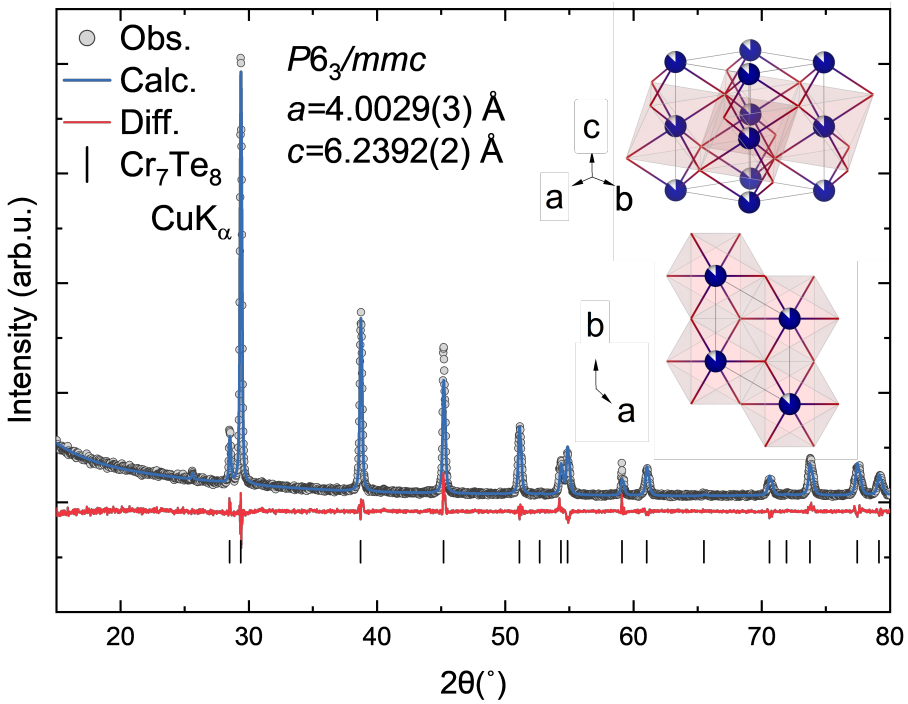

Figure 3.1: Crystal Structure of Cr_7Te_8 from the c-axis and crystal structure of Cr_7Te_8 detailing the Ni-As type structure with disordered chromium vacancies Rietveld refinement of Cr_7Te_8 using Cu K-α radiation. Residuals were 6.97%, the vertical tick marks represent the hexagonal unit cell.

increase in Bragg reflections is observed in the ordered phase Cr_7Te_8 which is indicative of the ordering of the chromium ions when allowed to naturally cool to room temperature upon synthesis. Powders looked similar upon ampule extraction and no obvious change in color or consistency was observed from the change in symmetry due to growth conditions. Several batches of Cr_7Te_8 were grown via solid state synthesis as they were used as the reactants in the following chapters single crystal growths and powder X-ray diffraction of the hexagonal phase often times showed inhomogeneities with small shifts in lattice parameters. I theorize this is due to the fast quenching process locking in slight differences in

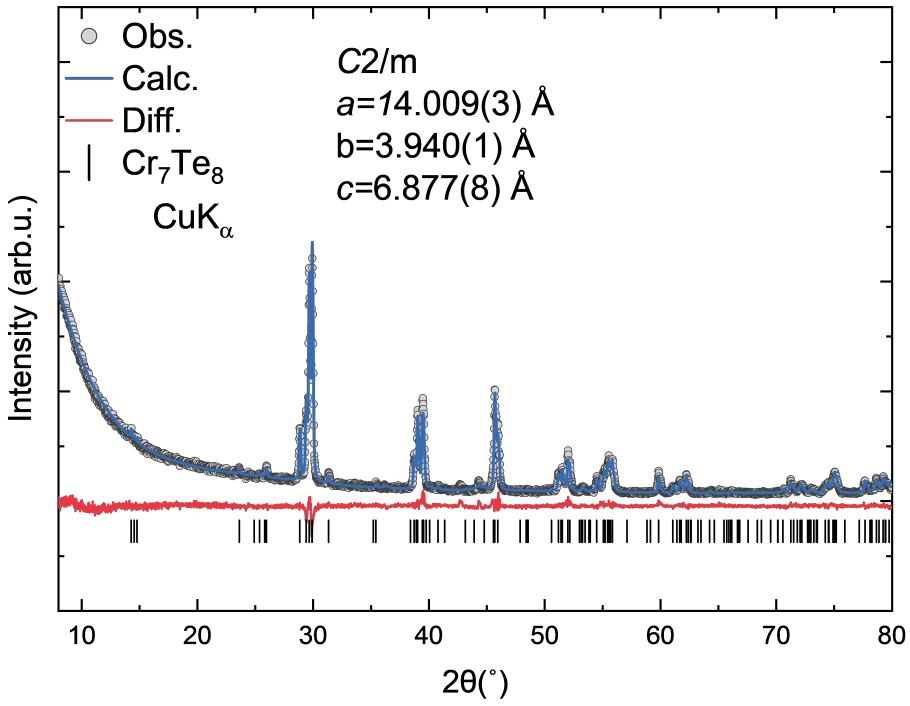

Figure 3.2: Powder X-ray diffraction pattern and Rietveld refinement of ordered phase Cr_7Te_8. Residuals were 6.193%, the vertical tick marks represent the monoclinic unit cell.

the thermodynamically stable phase. Too alleviate the existence of several different phases annealing was preformed on the powders to give a uniform phase. The disordered phase Cr_7Te_8 was taken from the original reaction vessel and finely ground and resealed in a quartz ampule where it was placed in a furnace for 24 hours at 1000°C. For the monoclinic phase the powders were removed from the ampule, finely ground and held at 400°C for 24 hours.

3.4 Synchrotron X-ray Diffraction

Previously mentioned the existence of peak splitting of Cr_7Te_8 was observed in laboratory powder X-ray diffraction and the need for annealing of samples was further confirmed via synchrotron X-ray diffraction at the I11-DLS beamline. Rietveld refinement and diffraction patterns of monoclinic and hexagonal Cr_7Te_8 are pictured below in figures 3.3

and 3.4. The hexagonal phase seems to have some monoclinic distortion which was originally thought to be inhomogeneities due to the resolution of the laboratory X-ray utilized. Figure 3.5 shows the ordered phase with one single phase due to the cooling process utilized upon solid state synthesis. Pictured above is a Rietveld refinement utilizing multiple

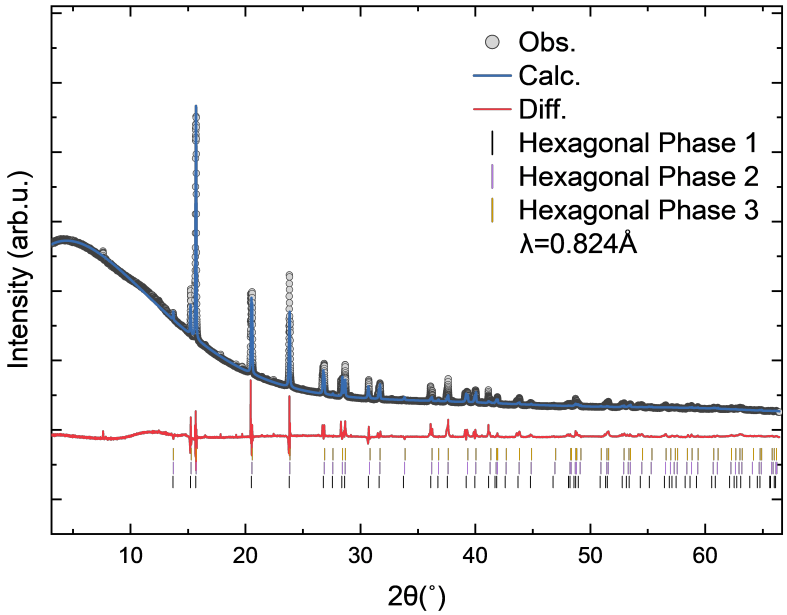

Figure 3.3: Synchrotron diffraction of hexagonal Cr_7Te_8 refined with three inhomogeneous hexagonal phases.

hexagonal phases to rule out the previously hypothesized inhomogeneities. A much better fit is observed when utilizing the monoclinic C2/m phase alongside the hexagonal phase. Phase fractions of 72% and 28% for the hexagonal and monoclinic phases were calculated via Rietveld refinement and a lower wR of 2.158% is calculated compared to the triple phased wR of 3.459%. Synchrotron data clearly shows the existence of a monoclinicly distorted hexagonal phase with low phase fractions. The first reports of the hexagonal phase Cr_7Te_8 likely did not have high enough resolution to sufficiently rule out monoclinic distortions to the hexagonal unit cell.[25] Due to this, the observed hexagonal phase is likely a thermodynamically meta-stable phase that is locked in via the quenching process. Isolating

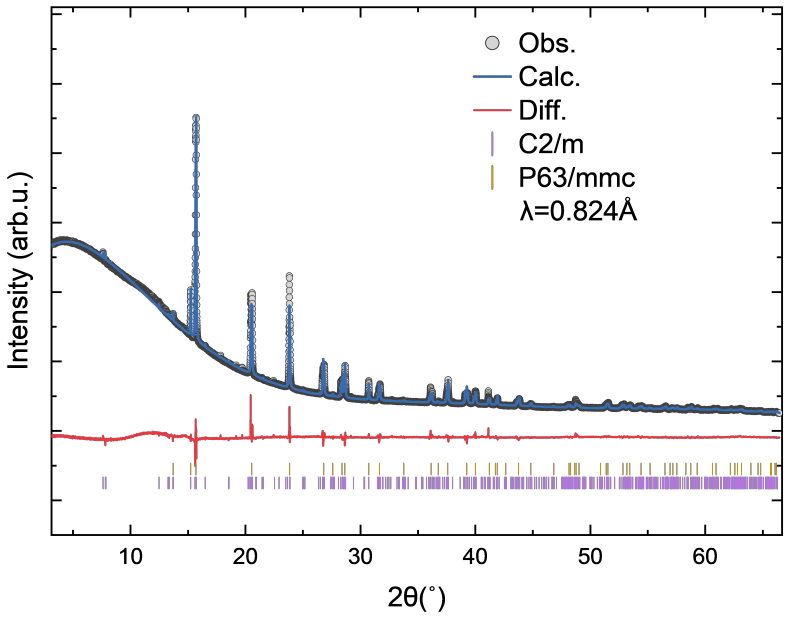

Figure 3.4: Synchrotron diffraction of hexagonal Cr_7Te_8 at I11-DLS showing monoclinic distortion. Rietveld refinement was preformed utilzing both monoclinic and hexagonal phases.

this phase in a single crystal phase is likely difficult or impossible due to the temperature gradient that would be utilized in the chemical vapor transport process. An ordering of the chromium will likely occur and form lower symmetry single crystal samples as will be proven in chapter 4. Rietveld Refinement utilizing the monoclinic C2/m phase on the slow cooled ordered phase Cr_7Te_8 results in wR of 2.796%. This again confirms the meta-stable nature of the disordered hexagonal phase and confirms the preferred phase of Cr_7Te_8 to be the ordered monoclinic phase. Isolation of a pseudo-hexagonal phase is possible via high temperature quenching of the solid state reaction vessel but some monoclinic distortions are still observed adding bragg reflections that can be defined using a monoclinic unit cell. Upon confirmation of the existence of the hexagonal meta-stable phase and the stable ordered phase, further magnetic studies were preformed to study the effect of chromium ordering on the overall magnetic structure of the chromium telluride compound.

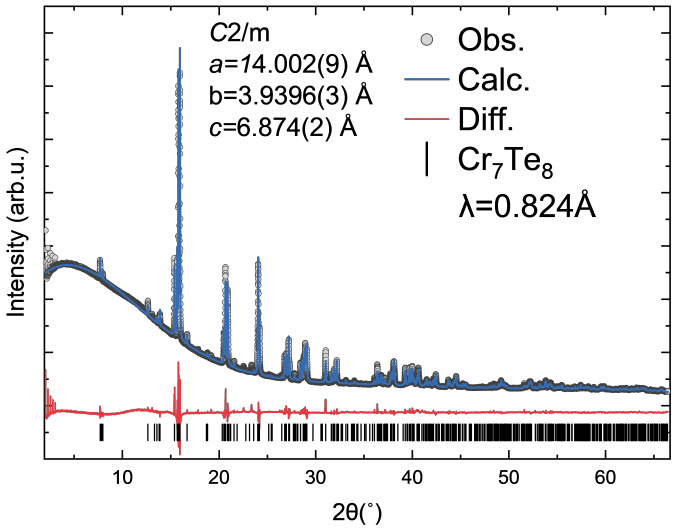

Figure 3.5: Synchrotron diffraction of monoclinic Cr_7Te_8 at I11-DLS showing a homogeneous sample. Vertical tick marks show allowed reflections for the monoclinic space group.

3.5 Magnetic Susceptibility

Magnetic susceptibility was preformed utilizing a vibrating sample magnetometer on both the monoclinic and meta-stable hexagonal Cr_7Te_8 polycrystalline samples. A paramagnetic to ferromagnetic transition is observed at roughly 342 K for the meta-stable hexagonal phase sample and 328 K for the monoclinic ordered sample. Figure 3.6 shows the hexagonal phase paramagnetic to ferromagnetic transition temperature. Ordering of the chromium in the crystal lattice presumably lowers the ferromagnetic transition temperature by roughly 5 K. This could be due to the addition of AFM producing chromium-chromium bonds in the c-lattice as hypothesized by DFT calculations. [19] Some octahedron distortion could also be the root cause of the lowered PM-FM transition but further studies on octahedral differences between ordered and disordered phases would need to be preformed. Magnetic susceptibility was also taken on both the monoclinic and hexagonal polycrystalline samples utilizing a SQUID from 2 K-400 K. Shown below in Figure 4.7, two metamagnetic transitions are observed in the hexagonal phase that are not observed in

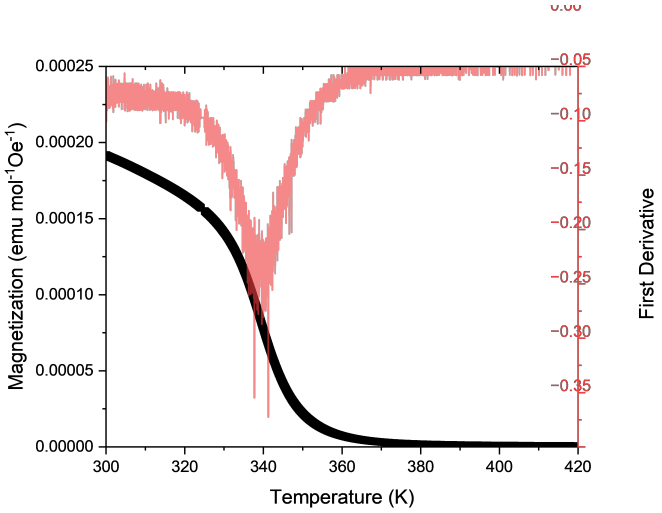

Figure 3.6: VSM magnetic susceptibility data showing the Curie temperature of 340 K for the Hexagonal Phase.

the monoclinic phase. Antiferromagnetic contributions to the magnetic moment seem to arise with the disordering of chromium in the crystal lattice compared to the single transition observed in the monoclinic phase pictured in Figure 3.8. Zhang et al hypothesized that with increasing chromium content the anti-ferromagnetic moment would be suppressed which seems to be more true with the ordered phase polycrystalline materials. However, the random distribution of chromium vacancies observed in the pseud-hexagonal phase must hae some impact on the increased anti-ferromagnetic contributions. [7] The ordered phase seems to resemble a simple ferromagnet when compared to the disordered phase where some amount of AFM-like behavior is observed. Typically chromium tellurides show simple ferromagnetic behavior above 200 K but metamagnetic transitions around 70 K-120 K are common as seen in monoclinic Cr_3Te_4 and Cr_5Te_8.[6, 7] In order to greater elucidate the paramagnetic to ferromagnetic transition field sweeps at varying temperatures were taken and Arrott plots were generated and will be discussed in the following chapter.

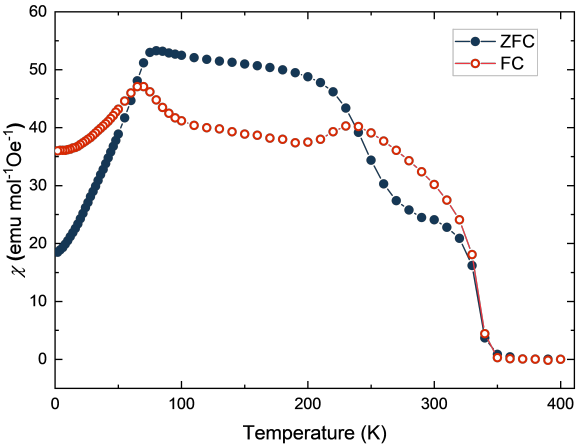

Figure 3.7: SQUID data showing the two meta-magnetic transitions of the hexagonal phase polycrystalline Cr_7Te_8. Meta magnetic transitions are observed at 250K and 70K.

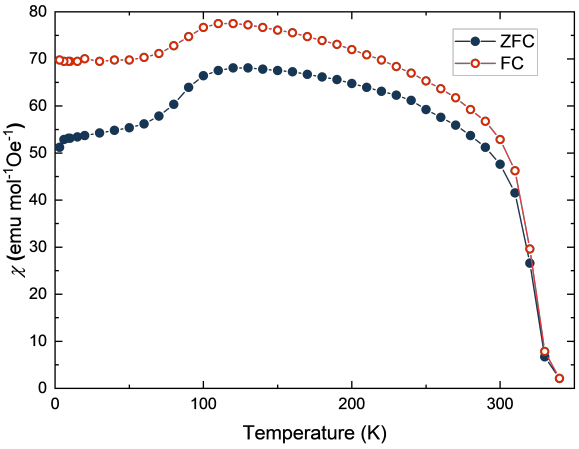

Figure 3.8: SQUID data showing the single magnetic transition of the monoclinic phase polycrystalline Cr_7Te_8.

3.6 Field Sweep

Arrott plots were generated from MvH loops to confirm the Curie temperature with greater confidence. Steps of 2 Kelvin were taken from 320 K to 370 K and fields were scanned from 4T to -4T. The data was plotted as $M^2 vs H/M$. Curves showing a linear region that when extrapolated proceed through the origin represent the true paramagnetic to ferromagnetic transition temperature. The temperature scans that are non-linear in shape

show the sample above or below the ferromagnetic transition temperature depending on their shape. Arrott plots pictured in Figure 3.9 below show the change in Curie temper-

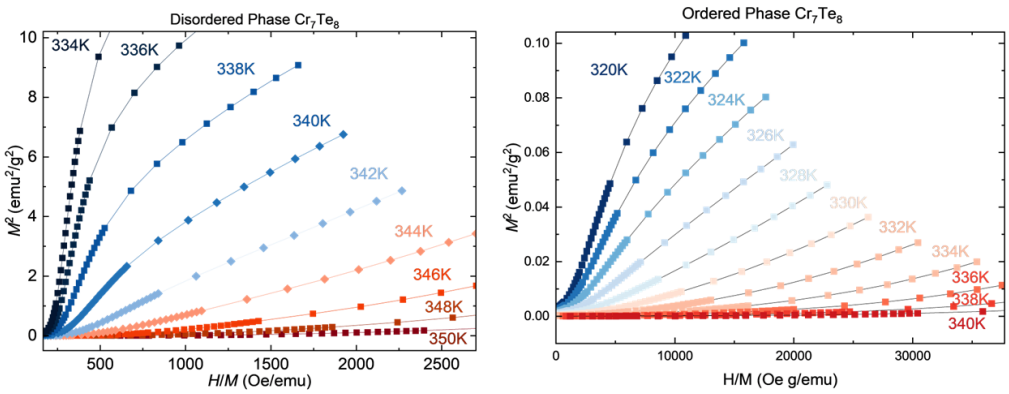

Figure 3.9: Arrott Plot of both Monoclinic (Ordered) and meta stable Hexagonal (Disordered) phase Cr_7Te_8.

ature of roughly 10 K-12 K showing a significant reduction of ferromagnetic transition temperature likely due to the ordering of chromium in the crystal lattice. As seen above field sweep measurements were preformed on the meta stable hexagonal and monoclinic Cr_7Te_8 and a change in hysteresis was observed in the monoclinic sample. An increase in hysteresis signifies the nature of the ferromagnet becomes harder and likely more usable than a soft ferromagnet like the disordered phase. However, it should be noted that the ordered phase, while harder than the disordered phase, is still primarily a soft magnet with easy switching compared to something like Fe_3GeTe_2. Figure 3.10 below shows the change in magnetic hysteresis between the hexagonal and monoclinic phases. Relatively small field of rough .5T are required for switching of the ordered phase chromium telluride and much lower than that for the disordered phase which shows no observable hysteresis. With the macro-magnetic properties studied, neutron diffraction was preformed on

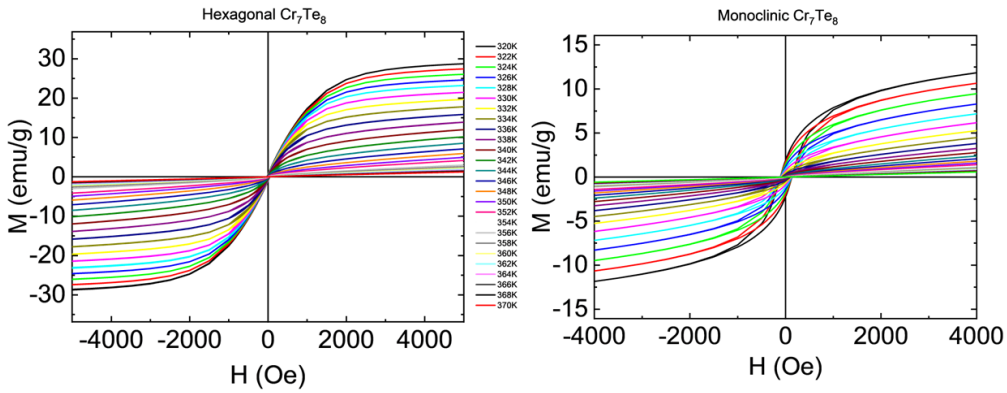

Figure 3.10: Monoclinic vs Hexagonal Hysteresis loops of Cr_7Te_8. Monoclinic phase Cr_7Te_8 shows greater fields required for switching indicating monoclinic phase is a harder ferromagnetic when compared to Hexagonal phase.

polycrystalline disordered phase to further understand the meta-magnetic transition around 70 K. Studies of the sample at room temperature were also preformed to determine if the AFM contributions can be seen at room temperature.

3.6.1 Neutron Diffraction

To investigate the magnetic structure of Cr_7Te_8 we employed the neutron powder diffraction technique on the high-resolution neutron powder diffractometer,BT-1, NIST, USA with $\lambda = 2.0785\ \AA$. Temperature dependent measurements were at 400 K, 298 K, 150 K, and 5 K. The magnetic structure was solved with the BT-1 Neutron powder diffraction data by analyzing the possible magnetic symmetries provided by k-SUBGROUPGMAGtool from the Bilbao Crystallographic Server within GSAS-II. 400 K measurements were utilized to solve the crystal structure of the sample sent for neutron diffraction. Due to the resolution of the BT-1 diffractometer, the meta-stable hexagonal phase was solved utilizing the

hexagonal $P6_3/mmc$ space group. Fits utilizing the monoclinic space groups resulted in

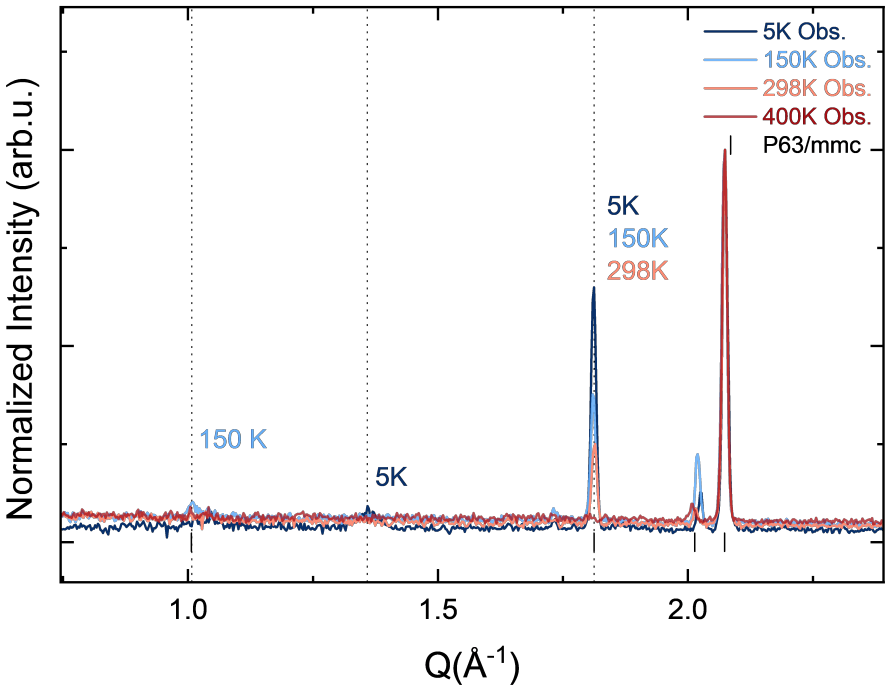

Figure 3.11: Normalized neutron diffraction data taken 400 K, 298 K, 150 K, and 5 K. Expected nuclear peak growth is observed at room temperature but symmetry disallowed peaks are observed around 1.01Åand 1.34Å.

worse weighted residuals because the peak splitting was not observed with the resolution the BT-1 allowed. However, for 150 K and 5 K refinements, the magnetic space group was dropped to the monoclinic $C2/c$ magnetic space-group. Figure 3.11 shows normalized raw diffraction data in low Q space to help identify the magnetic peak growth when temperature is lowered. Expected ferromagnetic growth of the nuclear peaks around 1.8 Å is observed upon lowering the temperature from 400 K to 298 K. However the emergence of a peak at roughly 1.01 Å is observed that can not be described by the original $P6_3/mmc$ space group. It can however be fit when the magnetic space group symmetry is dropped to the monoclinic phase, similar to that of the ordered phase. At 5 K a new magnetic peak is observed that was found to be due to a magnetic propagation vector of k vector of $(\frac{1}{2},\frac{1}{2},0)$. Figure 3.12 below shows the 400 K nuclear fit utilizing BT-1 data and the associated crystal

structure via the 3D visualization software VESTA. Due to no observable peak splitting the

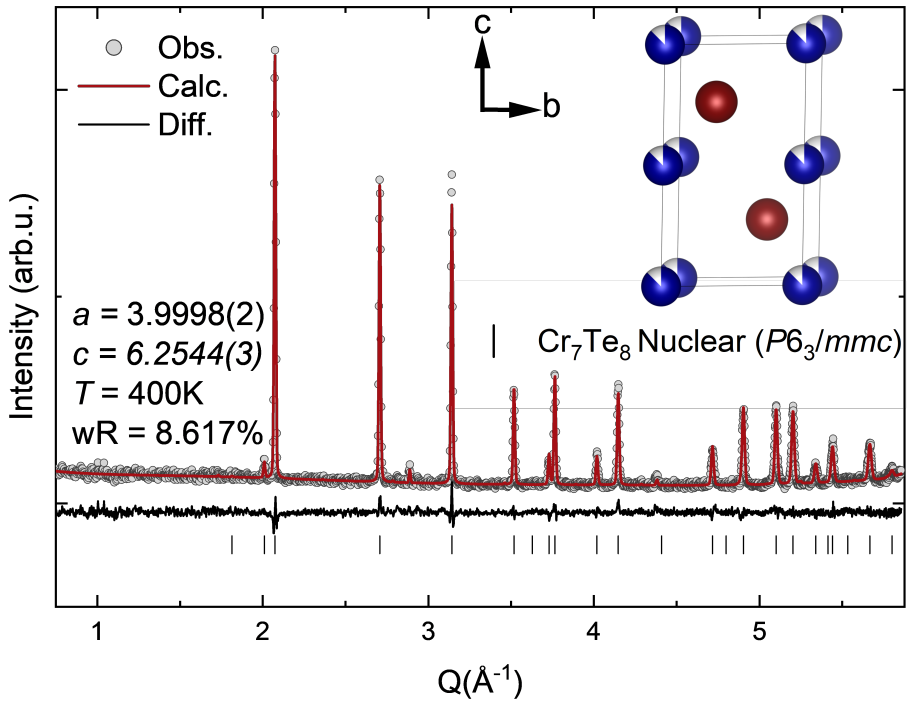

Figure 3.12: 400 K nuclear Rietveld refinement utilizing $P6_3/mmc$ space group due to BT-1 resolution. No observable peak splitting can be made out.

model used to fit the data was the high symmetry disordered phase. Weighted residuals of of 8.617% were observed and the crystal srtucture was solved to have lattice parameters of a =3.9998(2) Å and c =6.2544(3) Å.

Figure 3.13 shows the magnetic refinement for the disordered metastable hexagonal phase at room temperature. All observable peak growth was on symmetry allowed Bragg reflections signifying simple ferromagnetic ordering. Weighted residuals of 9.694% were observed and magnetic moments were calculated to be $M_z = 1.4559(28)\mu_B$. Lattice parameter refinements revealed an expansion in the a/b parameters to 4.0034(9) Å and a contraction in the c parameter to 6.24046(8) Å. Significant magnetic anisotropy was observed out of plane which aligns with reported neutron diffraction of monoclinic Cr_5Te_8 at room temperature.[21] Due to the monoclinic distortions observed we would anticipate similar

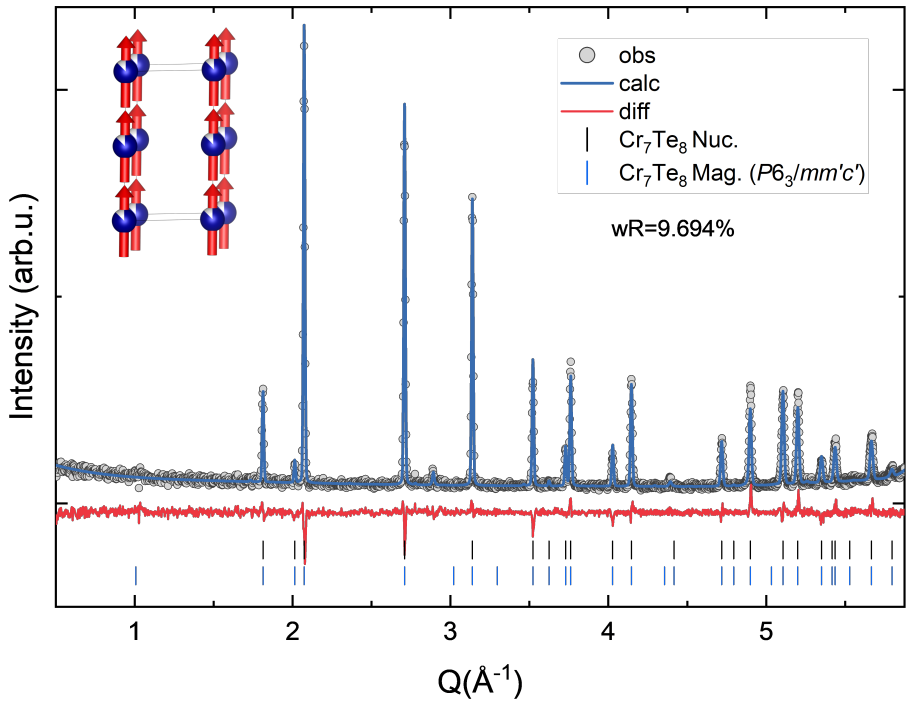

Figure 3.13: 298 K nuclear Rietveld refinement utilizing $P6_3/mmc$ space group due to BT-1 resolution. No observable peak splitting can be made out. Magnetic subgroup was solved to be $P6_3/mm'c'$ due to the ferromagnetic component in the c direction.

magnetic structure across the chromium telluride phase diagram as similar susceptibility data was also observed. Paramagnetic to ferromagnetic transition temperatures are lowered likely due to the lack of chromium content in Cr_5Te_8 but similar meta-magnetic transitions were observed.

A drop in symmetry was required to properly fit the 150 K neutron diffraction data due to the emergence of a symmetry disallowed peak when utilizing the $P6_3/mmc$ space group. A drop in symmetry to the monoclinic $C2/c$ phase allowed magnetic moment to be added to the peak at $1.04\AA^{-1}$. The reflection at $1.04\AA^{-1}$ is the (0,0,1) reflection and only sees growth when magnetic moment is added to the M_x moment direction. The solved magnetic structure shows a change in magnetic easy axis to the ab plane. Similar observations were seen in higher chromium content $Cr_{1-x}Te$ where as Hashimoto et al described

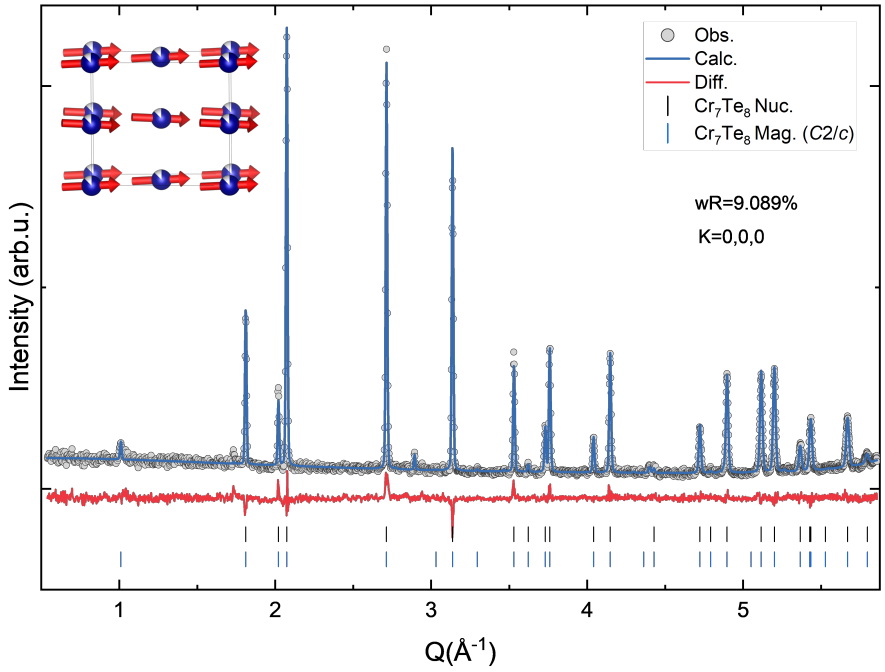

Figure 3.14: 150K nuclear Rietveld refinement utilizing $P6_3/mmc$ space group due to BT-1 resolution. No observable peak splitting can be made out. Magnetic subgroup was solved to be $C2/c$ with a change in ferromagnetic easy axis to the *ab* plane and the addition of AFM-like canting.

magnetic moment only along the *c*-axis.[66] Table 3.1 details the magnetic moment vec-

Table 3.1: Magnetic moment of chromium at 150 K solved from neutron diffraction, total magnetic moment is solved to be 2.93495.

M_x	M_y	M_z
0.6696	2.8480	0.2328

$$|\vec{M}| = \sqrt{M_x^2 + M_y^2 + M_z^2} \approx 2.93495\,\mu_B$$

tors for the chromium ions in the crystal structure. Total magnetic moments were solved to be $2.93495\,\mu_B$. When comparing with the magnetic susceptibility data preformed on the SQUID magnetometer, the alignment of the magnetic moment in the *ab* plane could help understand the metamagnetic transition observed around 80K. The solved magnetic structure also begins to see some moment canting in a pseudo AFM-like state. Again, when

looking at the magnetic susceptibility data in Figure 3.7 this could account for the drop in magnetic susceptibility observed upon cooling.

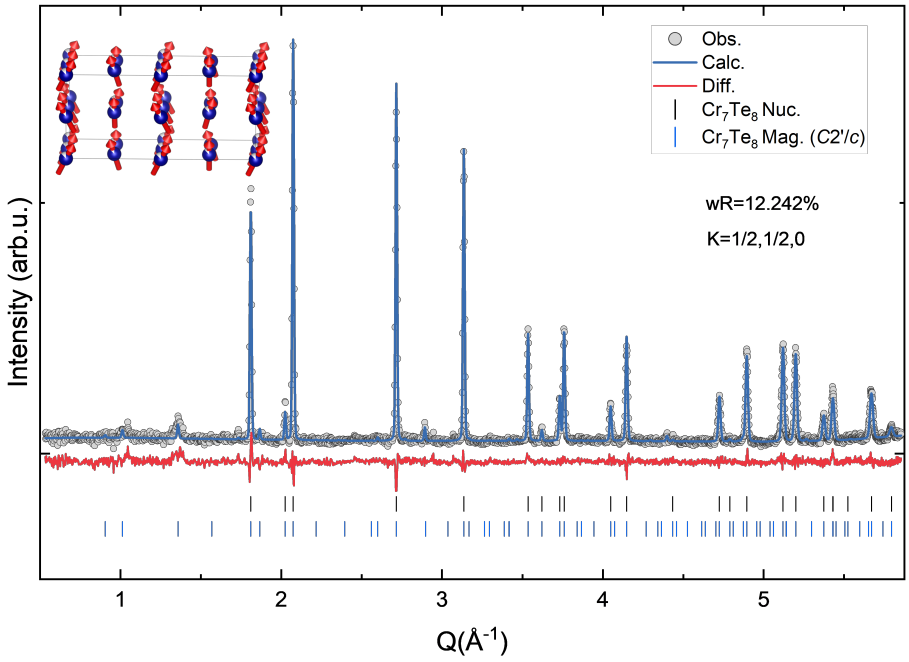

Figure 3.15: 5K nuclear Rietveld refinement utilizing $P6_3/mmc$ space group due to BT-1 resolution. No observable peak splitting can be made out. Magnetic subgroup was solved to be $C2'/c$ with a change in ferromagnetic easy axis back to the c axis and the addition of AFM-like canting.

Refinement of the 5 K data shown in Figure 3.15 shows another change in magnetic easy axis back to the c axis and the addition of a magnetic propagation vector of $k = (\frac{1}{2}, \frac{1}{2}, 0)$ Lattice parameter refinements revealed further expansion in the a/b lattice parameters to 4.00773(9) Å and an even more intense contraction sin the c lattice parameter to 6.20818(8) Å. The monoclinic space group was utilized to solve the magnetic structure and weighted residuals of 12.242% were realized. We hypothesize that the change in easy axis is attributed to the lattice parameter shift observed upon cooling. A propagation vector of $k = (0, 0, \frac{1}{2})$ also falls within an acceptable range to allow for moment growth at the new peak arising near 1.34 $\AA^{-1}$. However when attempting refinements utilizing this propaga-

Table 3.2: Magnetic moment of chromium at 5 K solved from neutron diffraction, average total magnetic moment is solved to be 2.9398

Atom	M_x	M_y	M_z	**Magnitude**
Cr 1	1.3601	0.0491	2.4890	2.4945
Cr 2	1.3601	0.6830	2.4890	2.4945
Cr 3	1.2774	1.1956	2.4890	2.4945
Cr 4	1.4234	1.1956	2.4890	2.4945
Total	5.4210	3.1233	9.9560	11.7590
Average	1.3553	0.7808	2.4890	2.9398

tion vector significantly worse goodness of fit scores are achieved. The Cr_7Te_8 meta-stable hexagonal phase seems to experience regular thermal contraction in the *c*-axis and expansion in the *a*/*b* plane. The change in orbital overlap of the Cr-Cr $3d_{z^2}$ orbitals and between the $Cr3_d$-Te5p orbitals likely is the main contributor to the exotic magnetism observed in the hexagonal system. Previous studies looking at tellurium and selenium substitution have shown that upon substitution of tellurium with selenium, the Chromium-selenide becomes increasingly more anti-ferromagnetic. This is likely due to the decrease in distance of chromium ions in the *c*-lattice.[67] Strain induced on chromium telluride systems also increases the FM to AFM behavior which again could be due to the decreased Cr-Cr distance in t the c-lattice. Due to our systems contraction in the c-lattice upon cooling, we can liken the observed behavior with strain in that direction.[67] The lack of metamagnetic transitions observed in the monoclinic system likely means that the ordering of chromium in the compound stabilizes some of these interactions and leads to a more typical ferromagnet. Future neutron diffraction studies should be preformed on the monoclinic phase Cr_7Te_8 sample to elucidate this hypothesis. It is possible the contraction of the closest Cr-Cr layer is lessened due to the ordering of closest neighbor chromiums.

A magnetic phase diagram generated from the magnetic susceptibility data and neutron diffraction refinements is pictured in Figure 3.16 and shows the simple ferromagnetic structure at 298 K, followed by a change in easy axis to the *a*/*b* plane. Finally, at 5 K the

magnetic moments realign to the c-axis and show some antiferromagnetic contributions.

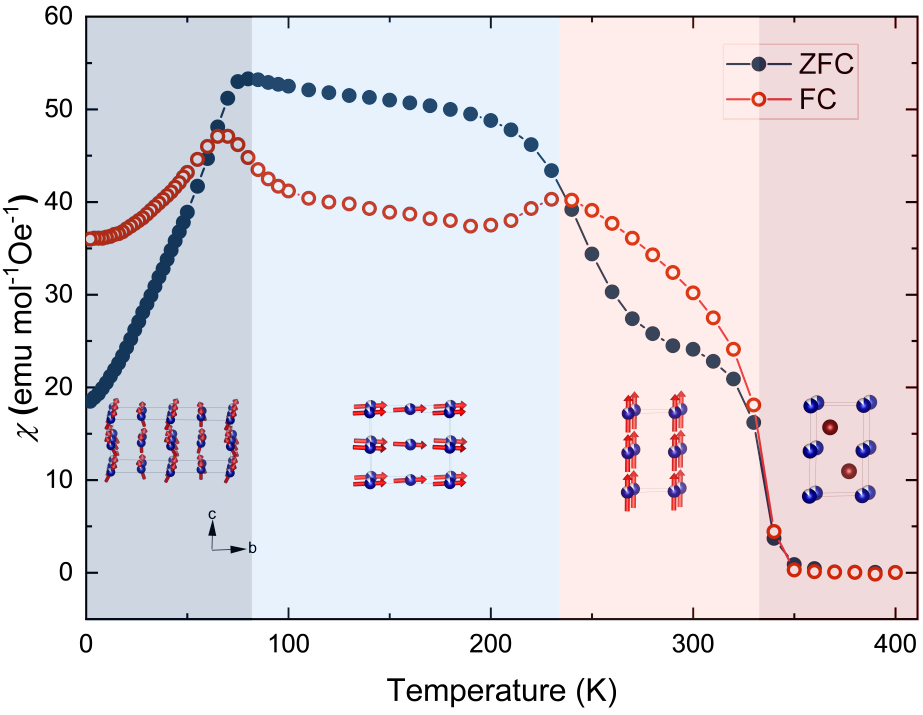

Figure 3.16: Phase diagram with the magnetic structures solved from BT-1 neutron diffraction.

Higher resolution single crystal neutron diffraction could be utilized to confirm the magnetic structure of the Cr_7Te_8 samples. The peak observed at 1.34 $\AA^{-1}$ proved difficult to fit with the resolution of the BT-1 instrument. While the fit pictured in Figure 3.15 fits the data well, there is some missing ferromagnetic intensity in the peak at 1.81 $\AA^{-1}$ that could not be accounted for without a total drop in symmetry and highly correlated refinement factors.

Contrary to Zhang et al's work showing AFM suppression with increasing chromium content, Anti-ferromagnetic moment can be seen in the polycrystalline Cr_7Te_8 which is nearing the top of the chromium boundary.[7] This leads us to believe that the chromium disorder and the potential lack of nearest neighbor Cr-Cr in the crystal lattice results in higher AFM contribution than hypothesized.[7] Zhang et al hypothesized with sufficient chromium content FM coupling would be enhanced but marked AFM behavior is still ob-

served in our polycrystalline Cr_7Te_8 neutron study.[7] Another study on $Cr_{1+x}Te_2$ and self-intercalated Cr-Cr effects on AFM transition temperatures was preformed and conclusions of decreased intercalated Chromium was directly related to increasing Neel temperature.[68] However, they suggest that decreasing chromium content in the crystal lattice increases ferromagnetic stability. This contradicts the tunability studies in $Cr_{5+x}Te_8$ leading to a possible symmetry argument for AFM moment rather than just chromium occupation.[7, 68] Another important interaction in the chromium telluride system is the reduction of inter-layer spacing in the *c*-lattice. Reduced inter-layer spacing may strengthen the Cr 3d and Tellurium 5p hybridization leading to stronger superexchange coupling. This super exchange coupling is highly dependent on bond distances and bond angles of the Cr-Te-Cr paths.[68] The neutron refinements of our Cr_7Te_8 sample shows a shrink in the c-lattice parameter which may help explain the exotic magnetism we observe in our system with the change in easy axis and addition of AFM component at low temperature.

Chapter 4: Magnetic Analysis of Chromium-Telluride Single Crystals

Chromium tellurides have an expansive and complex phase diagram with high dependency on chromium content and growth conditions.[69] In an attempt to grow the meta-stable hexagonal Cr_7Te_8 as a single crystal for single crystal neutron diffraction a variety of chromium telluride samples were synthesized and magnetic properties were explored via MPMS. Both magnetic susceptibility and field sweeps were preformed on the samples to explore the effect of chromium disorder and chromium content on the chromium telluride system. Similar metamagnetic transitions were observed in some space group symmetries that have been previously reported along with simple ferromagnetic samples, according to magnetic susceptibility data.Chemical vapor transport was utilized to grow single crystal samples utilizing meta-stable hexagonal Cr_7Te_8 charge powder. Charge powder was synthesized as stated in Chapter 3.1 and various growth conditions were utilized to explore the chromium rich chromium-telluride domain. Effects of quenching the sample during the CVT process were also studied to determine if quenching could lock in the high temperature thermal state.

4.1 Single Crystal Synthesis

Thirteen centimeter tubes utilizing $CrCl_3$ and I_2 as vapor transport agents were used and grown at temperatures ranging from 1000°C-950° for one-two week vapor transport growths. Flux growth methods were also utilized but didn't result in the formation of high

quality single crystals. In growth attempts utilizing iodine as the transport agent we noticed significant green color when washing with ethanol and water. This was attributed to the in-situ synthesis of chromium iodide and often resulted in lesser chromium content in the single crystal samples. Due to this observation we utilized additional elemental chromium alongside the charge powder to account for the chromium iodide formation upon crystallization. The samples that utilized elemental chromium did result in higher chromium content in the crystal lattice but still often was short of the Cr_7Te_8 target phase. Several single crystal compositions were grown utilizing the hexagonal Cr_7Te_8 and are tabulated in Table 4.1.

Table 4.1: Summary of crystal growth experiments.

Experiment ID	Starting Powder	CVT Agent	Temperature	Composition of Single Crystal	Space Group
TRA014A	500 mg Cr_7Te_8	100 mg I_2	1000°C	$Cr_{5.38}Te_8$	Non-centrosymmetric $P\bar{3}m1$
TRA015A	1.0 g Cr_7Te_8 and 20 mg Cr	80 mg I_2	950°C	$Cr_{5.85}Te_8$	Monoclinic C2/m
TRA023B	1.0 g $Cr_{7.4}Te_8$	60 mg I_2	965°C	$Cr_{6.22}Te_8$	P3
TRA028A	1.0 g $Cr_{7.4}Te_8$	80 mg I_2	1000°C	$Cr_{6.66}Te_8$	$P\bar{6}m2$

Crystals with compositions of monoclinic, trigonal, non-centrosymmetric trigonal, and hexagonal were formed. Particularly interesting is the hexagonal phase grown with composition of $Cr_6.66Te_8$ or better represented as $Cr_6.29Te_7.55$ as some tellurium disorder was also apparent. Typically only chromium disorder is seen but attempts of quenching to maintain chromium disorder resulted in tellurium displacement which is not typically seen in the solid state synthesis of the charge powder. As mentioned in DFT calculations Cr3d-Te5p covalencey plays an important role in the chromium-telluride magnetic structure so introducing tellurium vacancies could alter the magnetic state similarly to chromium disorder. Due to new space groups being formed that have not yet been explored, macro magnetic properties were measured utilizing the SQUID magnetometer. Confirmatory single crystal X-ray diffraction was also utilized to confirm the crystal structure as well as electron dispersive X-ray spectroscopy. Raman spectroscopy was also used to determine if chromium content in the single crystal could be quickly identified via a shift in Raman bands but no

observable pattern was seen.

4.2 Single Crystal X-ray Diffraction

The structure of the single crystal samples were confirmed by single crystal X-ray diffraction utilizing molybdenum $K\alpha$ radiation. Compositions of Non-centrosymmetric P$\bar{3}$m1, Monoclinic C2/m, trigonal P3 and Hexagonal P$\bar{6}$m2 were successfully synthesized. Slight variations in Chromium filling in the partially filled layers gives a wide variety of crystal structures that seems to have great impact on macro-magnetic properties.

Table 4.2: Single Crystal Results for $Cr_{5.86}Te_8$ with space group $C2/m$. Estimated standard deviations are given in parentheses.

Property	Value
Space Group	C2/m
a (Å)	14.0360(8)
b (Å)	3.9429(2)
c (Å)	6.8730(4)
β (deg)	118.354(2)
Crystal System	Monoclinic
Volume (Å^3)	334.74(3)
Z	1
Λ (Mo Kα) (Å)	0.71073
No. of Reflections Collected	4732
F(000)	557
Final R Indexes (all data)	WR = 0.0463
Temperature (K)	298(2)

Table 4.2 above shows the crystals lattice parameters and other single crystal refinement parameters. The monoclinic crystal still orders in chromium full and chromium deficient layers. However, there seems to be a preferred sight of richer chromium occupation among the crystal lattice. Chromium that occupies the chromium three site is occupied at a rate of roughly 4% and this seems to be where the monoclinic distortion arises from. In the higher symmetry crystal structures chromium in the non-fully occupied layer doesn't have a

preferred site but with increasing chromium content a distortion of the octahedron happens and a preferred sight is formed.

Table 4.3: Atomic Parameters Table for Monoclinic $Cr_{5.86}Te_8$.

Name	Type	x	y	z	frac	site sym	mult	I/A
Te1	Te	0.36800	0.50000	0.03144	1.0000	m(y)	4	A
Te2	Te	0.11950	0.50000	0.45475	1.0000	m(y)	4	A
Cr1	Cr	0.25555	0.50000	0.27406	1.0000	m(y)	4	A
Cr2	Cr	0.00000	0.50000	0.00000	0.8890	2/m(y)	2	A
Cr3	Cr	0.50000	0.50000	0.50000	0.0400	2/m(y)	2	I

VESTA 3D crystal visualization software was used to generate a 3D view of the monoclinic crystal structure to help aide in the understanding of the chromium rich and chromium deficient layer. Chromium 1 in the atom parameters table above shows the chromium full site locations with the specific wyckoff positions of x =.368, y = .500 and z = .03144. As the crystal lattice expands in the a direction chromium deficient layers form after the chromium rich layer and two unique chromium sites are formed corresponding to chromium 2 and chromium 3 in Table 4.3. Figure 4.1 shows the monoclinic unit cell doubled in size to portray the chromium deficient and chromium full layering structure. The chromium deficient layer with two distinct chromium sites can be seen in the VESTA image and the slight distortion of the octahedrons can be seen when compared to the higher symmetry crystal structures.

The next single crystal that was produced via chemical vapor transport is the non-centrosymmetric $P\bar{3}m1$. The single crystal has less chromium in the crystal lattice and has a composition of $Cr_{5.38}Te_8$. The chromium orders in fully deficient and full stacking layers with no preferred chromium site on the deficient layer like seen in the monoclinic phase discussed previously. In the trigonal $P\bar{3}m1$ crystal the chromium stacks alternating between chromium full and chromium deficient layers in the c-axis. Unlike in the monoclinic unit cell no distortion of the octahedron stacking can be observed and is likely why

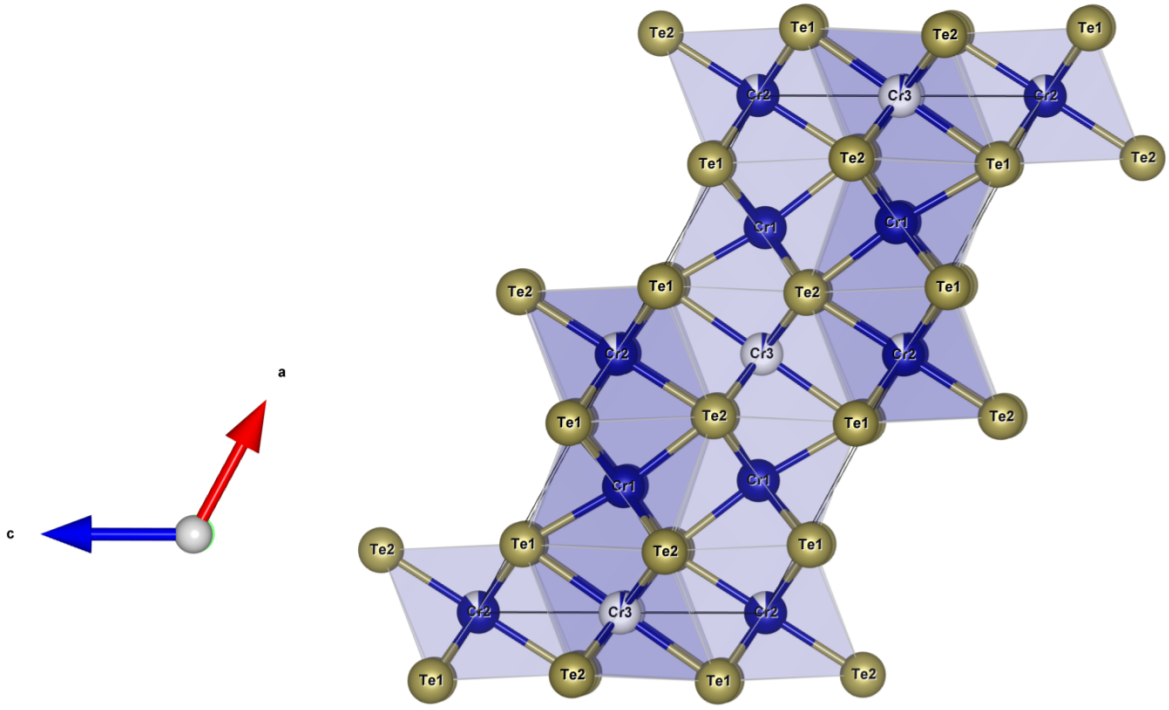

Figure 4.1: Crystal structure of the monoclinic *C*2/*m* $Cr_{5.86}Te_8$ made using VESTA crystal visualization software. Blue represents fractional occupancy of the chromium site and gray represents the chromium deficiency. A 75% blue circle shows 75% fractional occupancy.

the unit cell maintains a high level of symmetry. As seen above in Table 4.5 chromium 1 shows 100% chromium occupancy and the chromium 2 layer above shows roughly 34% chromium occupancy. The crystal lattice still shows close packed tellurium and chromium in the octahedron but there is no preferred chromium site in the deficient layers. The lack of preferred chromium sites likely will contribute to the magnetic properties of the sample and will be explored in sections below. Overall we are anticipating lower Curie temperatures due to the sample being overall less chromium rich with a composition of $Cr_{5.38}Te_8$. VESTA 3D visualization software was again utilized to show a 3D image of the crystal structure and was expanded to two unit cells to visualize the chromium full and chromium

Table 4.4: Crystallographic Data for Single Crystal $Cr_{5.38}Te_8$ with Space Group $P3m1$. Estimated standard deviations are given in parentheses.

Property	Value
Space Group	$P\bar{3}m1$
a (Å)	3.93415(14)
b (Å)	3.93415(14)
c (Å)	6.0938(3)
β (deg)	90
Crystal System	Trigonal
Volume (Å^3)	81.681(7)
Z	1
Λ (Mo Kα) (Å)	0.71073
No. of Reflections Collected	2111
F(000)	136.3
Final R Indexes (all data)	WR = 0.0447(328)
Temperature (K)	298(2)

Table 4.5: Atomic Positions for Space Group $P\bar{3}m1$

Name	Type	x	y	z	frac	site sym	mult	I/A
Te1	Te	0.00000	0.00000	0.24610	1.0000	3m(100)	1	A
Te2	Te	0.66667	0.33333	0.74545	1.0000	3m(100)	1	A
Cr1	Cr	0.33333	0.66667	0.49720	1.0000	3m(100)	1	A
Cr2	Cr	0.33333	0.66667	0.99800	0.3440	3m(100)	1	A

deficient stacking layers. No distortion of the octahedron layers can be observed and is likely why the crystal structure can be solved to a higher symmetry space group with single crystal X-ray diffraction. One other important note is that with both the monoclinic and trigonal structures no disorder is observed in the tellurium ions. However, disorder is observed in the hexagonal crystal that was produced via quenching that will be discussed below.

Another trigonal crystal with much higher chromium content was synthesized utilizing less Iodine as a transport agent. Slightly lower temperature conditions were also utilized with the hot end of the tube being at 965°C. The composition of the single crystal was solved to be $Cr_{6.22}Te_8$ with a space group of P3. Table 4.6 details the single crystal XRD

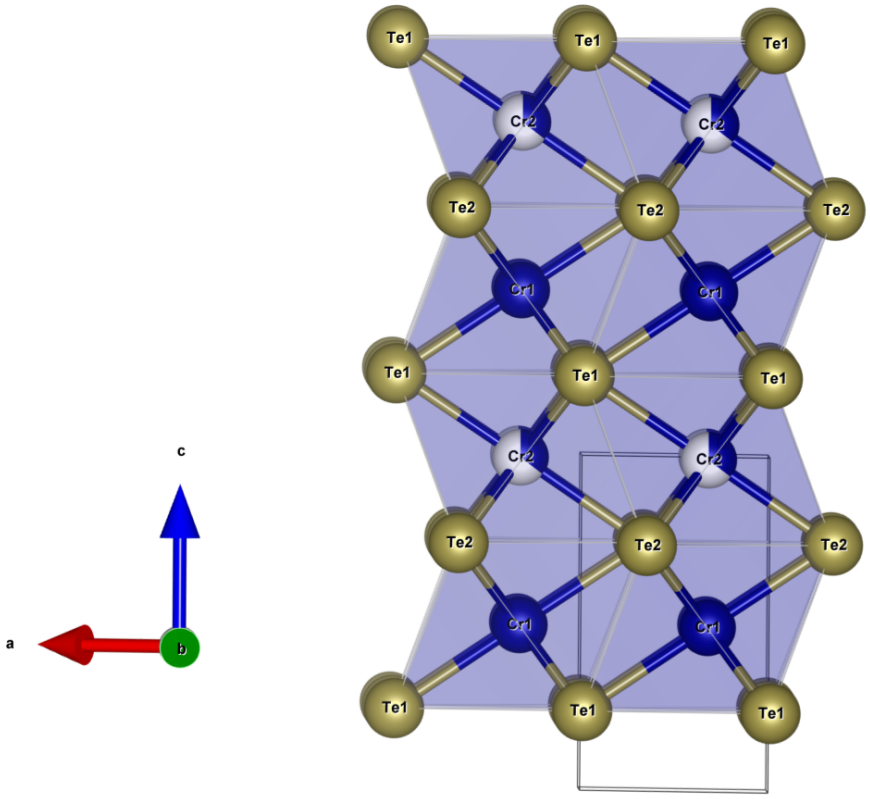

Figure 4.2: Crystal structure of the trigonal $P3m1$ symmetry $Cr_{5.38}Te_8$ made using VESTA crystal visualization software.

results from the single crystal sample. The unit cell is roughly doubled like that observed in the monoclinic single crystal but still holds the trigonal symmetry like that observed in the $P\bar{3}m1$ sample. Like the other related single crystals discussed previously chromium again stacks in chromium full and chromium deficient layers. However, in the $Cr_{6.22}Te_8$ single crystal several different unique chromium sites were solved with varying degrees of chromium occupation. Table 4.7 shows the vast chemically unique chromium sites of the $Cr_{6.22}Te_8$ single crystal sample. Due to the unique chromium ordering in the sample complex magnetic transitions are anticipated with meta-magnetic transitions like observed in the meta-stable hexagonal polycrystalline phase. Limited intra-layer distortions are seen

Table 4.6: Crystallographic Data for $Cr_{6.22}Te_8$ single crystal with Space Group P3. Estimated standard deviations are given in parentheses.

Property	Value
Space Group	P3
a (Å)	7.9551(4)
b (Å)	7.9551(4)
c (Å)	12.4149(9)
β (deg)	90
Crystal System	Trigonal
Volume ($Å^3$)	680.40(8)
Z	2
Λ (Mo Kα) (Å)	0.71073
No. of Reflections Collected	4646
F(000)	1131
Final R Indexes (all data)	WR = 0.0865
Temperature (K)	298(2)

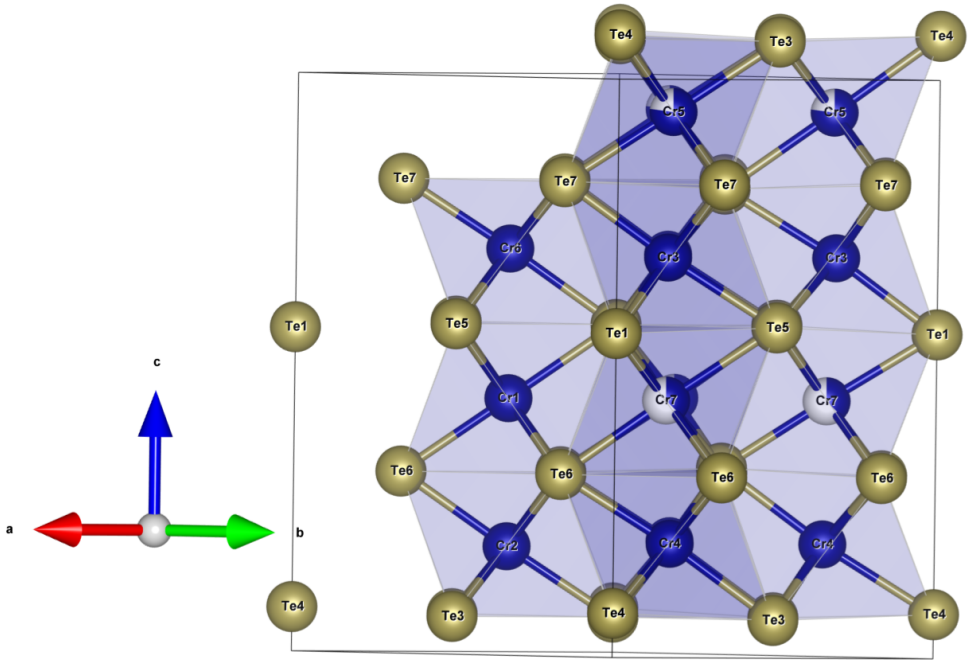

Figure 4.3: Crystal structure of the trigonal *P*3 Symmetry $Cr_{6.22}Te_8$ made using VESTA crystal visualization software. *P*3 Symmetry.

Table 4.7: Atomic Positions for Space Group P3

Name	Type	x	y	z	frac	site sym	mult	I/A
Te1	Te	0.00000	0.00000	0.56022	1.0000	3	1	A
Te2	Te	0.33333	0.66667	0.80759	1.0000	3	1	A
Te3	Te	0.49953	-0.00099	0.06530	1.0000	3	1	A
Te4	Te	0.00000	0.00000	0.07644	1.0000	3	1	A
Te5	Te	0.50050	0.00103	0.57114	1.0000	3	1	A
Te6	Te	0.33460	0.16719	0.31305	1.0000	3	1	A
Te7	Te	0.32320	0.16599	0.19713	1.0000	3	1	A
Te8	Te	0.33333	-0.33333	0.32520	1.0000	3	1	A
Cr1	Cr	0.66667	0.33333	0.44140	1.0000	3	1	A
Cr2	Cr	0.66667	0.33333	0.18540	1.0000	3	1	A
Cr3	Cr	0.15880	0.31730	0.69040	1.0000	3	1	A
Cr4	Cr	0.17430	-0.17020	0.19550	1.0000	3	1	A
Cr5	Cr	0.15790	-0.17070	0.94210	0.7730	3	1	A
Cr6	Cr	0.66667	0.33333	0.71000	1.0000	3	1	A
Cr7	Cr	0.65840	-0.18330	0.44320	0.3760	3	1	A

in the case of the P3 symmetry unlike what we observe in the monoclinic space group. No observations of the P3 space group have been reported in literature. The chromium telluride phase diagram is complex so its possible this is an entirely new space group observed but further study and replication should be preformed to confirm the synthesis.

The final and highest symmetry crystal structure grown via CVT synthesis was a growth that recorded P$\bar{6}$m2 symmetry. The structure was solved via single crystal X-rays and the information is recorded in Table 4.8 below. This CVT growth utilized a quenching process from 1000°C similar to that utilized in growing the polycrystalline disordered phase. The quenching process was used to attempt to lock in the meta-stable hexagonal phase that is observed in polycrystalline samples. One interesting effect of quenching the CVT growth is that tellurium vacancies were introduced into the crystal lattice that have not been observed in any of the previous growths. Typically tellurium orders in a close packing nature with no vacancies and the only vacancies observed are from the chromium not filling in the octahedral sites. One other interesting effect of quenching is that the chromium full and

Table 4.8: Crystallographic Data for $Cr_{6.66}Te_8$ Single Crystal with Space Group $P\bar{6}m2$. Estimated standard deviations are given in parentheses.

Property	Value
Space Group	$P\bar{6}m2$
a (Å)	7.9995(3)
b (Å)	7.9995(3)
c (Å)	12.4804(7)
β (deg)	90
Crystal System	Hexagonal
Volume ($Å^3$)	691.65(6)
Z	2
Λ (Mo Kα) (Å)	0.71073
No. of Reflections Collected	5647
F(000)	1083.1
Final R Indexes (all data)	WR = 0.1108(914)
Temperature (K)	298

chromium deficient layers are not organized in entirely full and entirely vacant layers. The quenching seems to introduce vacancies on each of the layers with the normally ”full” layers containing less vacancies, but still some level of vacancies. No fully occupied layers are observed due to the quenching process and the locking in of the vacancies in both chromium and tellurium sites. Interestingly, Tellurium actually does form full and deficient alternating layers that until this growth, was only observed in chromium sites. Table 4.9 shows the atomic positions refined from single crystal X-ray diffraction.

Tellurium sites 5 and 6 show fractional occupancies of 89% and 87%. All chromium sites have some amount of disorder ranging from 65% fractional occupancy to 92% occupancy. The vacancies lead to a higher symmetry crystal structure similar to what having vacancies do in the polycrystalline samples synthesized in chapter 3. No inter layer distortions are observed similar to the trigonal crystals grown. Macro magnetic properties will be measured and the impact of the octahedron distortions will be elucidated.

All of the above synthesized crystal structure contain chromium full and chromium deficient layer stacking except when disorder is intentional introduced via quenching as

Table 4.9: Atomic Positions and Site Symmetry for Space Group P$\bar{6}$m2

Name	Type	x	y	z	frac	site sym	mult	I/A
Te1	Te	0.83292	0.66585	0.50000	1.0000	mm2(120)	3	A
Te2	Te	0.33333	0.66667	1.00000	1.0000	-6m2(100)	1	A
Te3	Te	0.33333	0.66667	1.00000	1.0000	-6m2(100)	1	A
Te4	Te	0.83382	0.66763	1.00000	1.0000	mm2(120)	3	A
Te5	Te	0.49977	0.50023	0.75221	0.8920	m(110)	6	A
Te6	Te	1.00000	1.00000	0.74368	0.8770	3m(100)	3	A
Cr1	Cr	0.66667	0.33333	0.62603	0.9230	3m(100)	3	A
Cr2	Cr	0.67360	0.83680	0.87580	0.8260	m(010)	6	A
Cr3	Cr	0.5990	0.82995	0.62160	0.7450	m(010)	6	A
Cr4	Cr	0.66667	0.33333	0.88010	0.6530	3m(100)	3	A

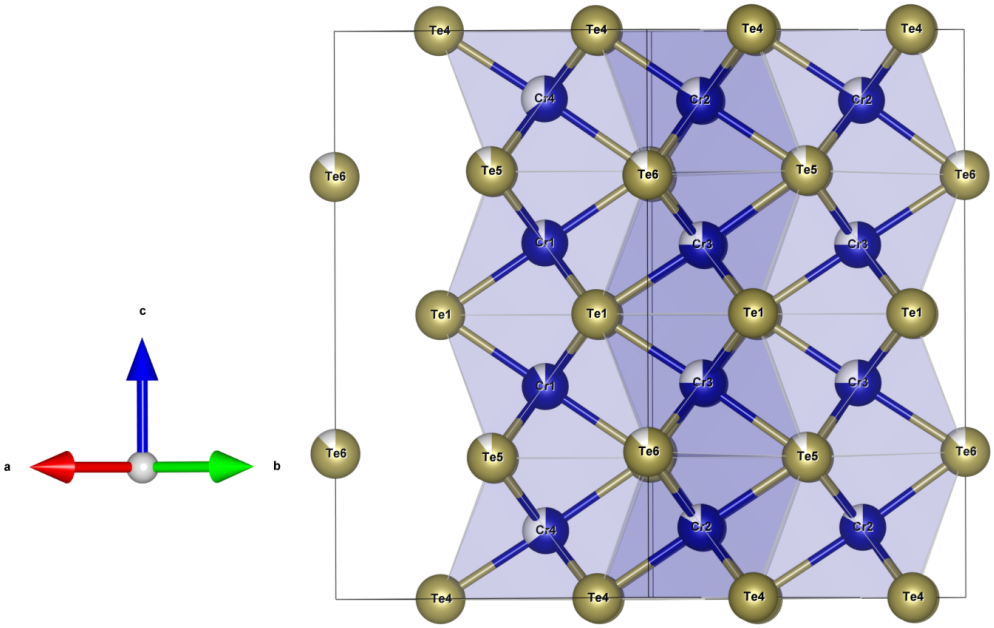

Figure 4.4: Crystal structure of the hexagonal $Cr_{6.66}Te_8$ with $P\bar{6}m2$ symmetry, made using VESTA crystal visualization software.

observed in the $Cr_{6.66}Te_8$. During the quenching process disorder is also introduced in the tellurium sites and may cause interesting magnetic phenomena due to the Cr-Te covalencey. Four unique Chromium sites and six unique tellurium sites were observed with single crys-

tal X-ray diffraction which is a significant increase when compared to the polycrystalline hexagonal sample.

Measurements of the magnetic properties of the single crystals were observed using the MPMS measurement tool and field sweeps and susceptibility data was collected. Comparison of chromium content and crystal symmetry on the magnetic properties was made to discover the most applicable pseudo 2D material for potential device fabrication. Thickness of samples was not measured prior to taking magnetic property measurements but should be considered in future studies due to the finding in Wen et al's work of increased Curie temperature with decreasing sample thickness.[2]

4.3 Magnetic Properties of Single Crystal Samples

Magnetic susceptibility data was taken on a quantum design MPMS from 2 K-315 K for the single crystal samples utilizing fields of 100 Oe. Both in and out of plane measurements of the crystals were taken but were not correlated with lattice directions due to the Laue diffractometer being down. Susceptibility data above 315 K was taken on a vibrating sample magnetometer due to the SQUIDS heating limitations.

The monoclinic Single crystals with compositions $Cr_{5.86}Te_8$ and space group $C2/m$ are room temperature ferromagnets with relatively weak hysteresis loops. One metamagnetic transition is recorded around 70 K and has been reported in previous work. [20] An observed change in easy axis has also been recorded similar to what was solved in the polycrystalline Cr_7Te_8 meta-stable hexagonal phase. [14] While susceptibility data and ESR has been used no single crystal neutron diffraction has been preformed and that is the logical next step for fleshing out the monoclinic magnetic structure. Figure 4.5 is the in-plane magnetic susceptibility data of the $Cr_{5.86}Te_8$ $C2/m$ single crystal. Significant FC and ZFC splitting is observed in the susceptibility measurements. While the ZFC line does

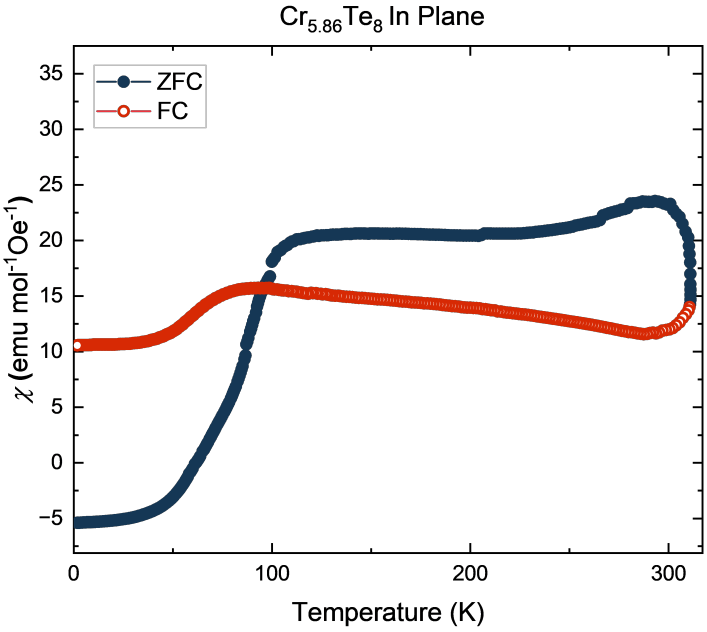

Figure 4.5: In-plane Magnetic Susceptibility of the $Cr_{5.86}Te_8$ single crystal sample. Paramagnetic to ferromagnetic transition can not be observed dude to the limitations of the MPMS but it is expected to be above room temperature around 320 K. The meta-magnetic transition around 70 K can be observed.

start with negative susceptibility it was determine the crystal likely had a majority of its ferromagnetic domains aligned mainly opposite to the plane chosen as our positive field. This resulted in what looked like superconducting behavior but was discovered not to be a super conducting sample. Splitting is also observed due to the simple ferromagnetic structure at high temperature and the inability of the SQUID to get to paramagnetic transition temperature. Due to this splitting of the ZFC and FC susceptibility curves will be observed in all of the single crystal samples below. Field sweep measurements pictured in Figure 4.6 show exotic in-plane magnetism with a hysteresis loop developing at 2 K, exotic negative magnetization at 120 K and normal soft ferromagnetic behavior at 300 K. The splitting observed at 300 K is likely due to some difference in ferromagnetic domains. It is possible the change in magnetization could be due to the thickness of the sample. It has already been

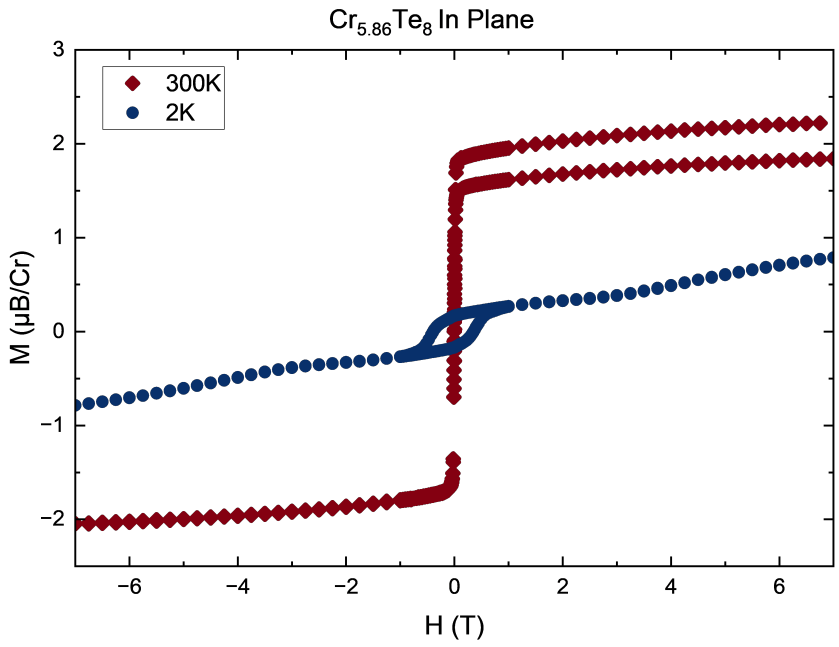

Figure 4.6: A slight hysteresis loop is observed at 2 K and simple soft ferromagnetic behavior is observed at 300 K.

reported that unique surface interactions occur that are similar to doping of the material. However, crystal thickness measurements were not preformed on the sample to determine if it was nearing the 2D domain. [2] Out of plane measurements were also taken on the monoclinic $Cr_{5.86}Te_8$ single crystal and the observed easy axis of the ferromagnetic moment was shown to be in the in-plane direction due to much higher magnetic saturation in the in-plane susceptibility data. The same single crystal sample was utilized for both in-plane and out of plane measurements to minimize possible differences among samples. One stark difference between in and out of plane samples is the difference in FC and ZFC splitting observed in the monoclinic sample. Higher ZFC saturation values are recorded in the in-plane samples compared to the opposite happening in the out of plane samples. Similar observations are seen in Jiang et al's work with Cr_5Te_8 monoclinic samples and is attributed to a spin flop behavior of the AFM-like moments. [70] Thermal contractions

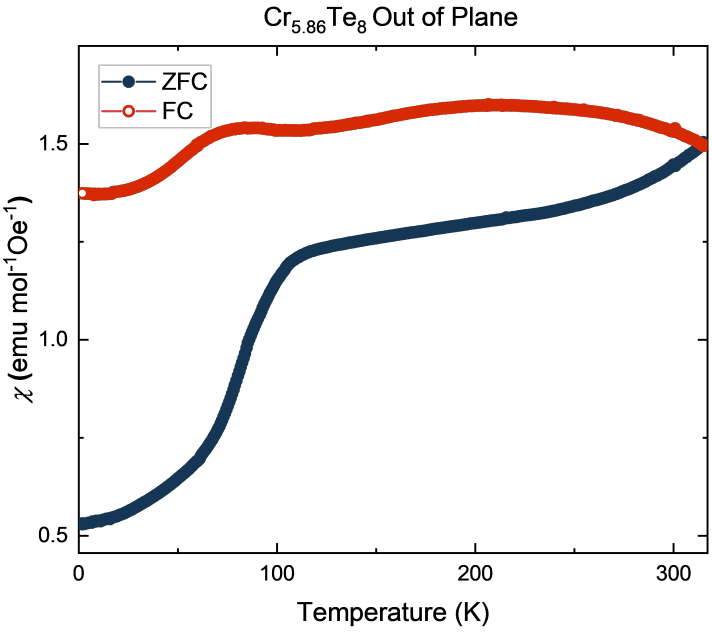

Figure 4.7: Out of plane Magnetic Susceptibility of the monoclinic $Cr_{5.86}Te_8$ single crystal sample. Paramagnetic to ferromagnetic transition can not be observed dude to the limitations of the MPMS but it is expected to be above room temperature around 330 K. The meta-magnetic transition around 70 K can still be observed like in the in-plane measurements. Lower saturation of the moments provides evidence that the magnetic easy axis is in-plane.

causing Cr-Cr inter layer distances to decrease is hypothesized as the cause for lessened AFM behavior in the monoclinic $Cr_{5+x}Te_8$ crystals. Compared to the higher symmetry single crystals less of a metamagnetic transition si observed at 70 K and more simple ferromagnetic behavior is observed. In contrast when more Cr-Cr interactions are observed due to higher chromium content a more intense meta-magnetic transition is observed as shown in the polycrystalline neutron diffraction in chapter 3. To develop a better understanding of the chromium rich Cr_5Te_8 monoclinic crystals neutron diffraction should be preformed and a clearer micro-magnetic understanding can be developed.

Trigonal $Cr_{5+x}Te_8$ with x=.38 were also synthesized and macro-magnetic properties were observed utilizing the MPMS from 2 K-315 K. Figure 4.9 shows a sharp increase in

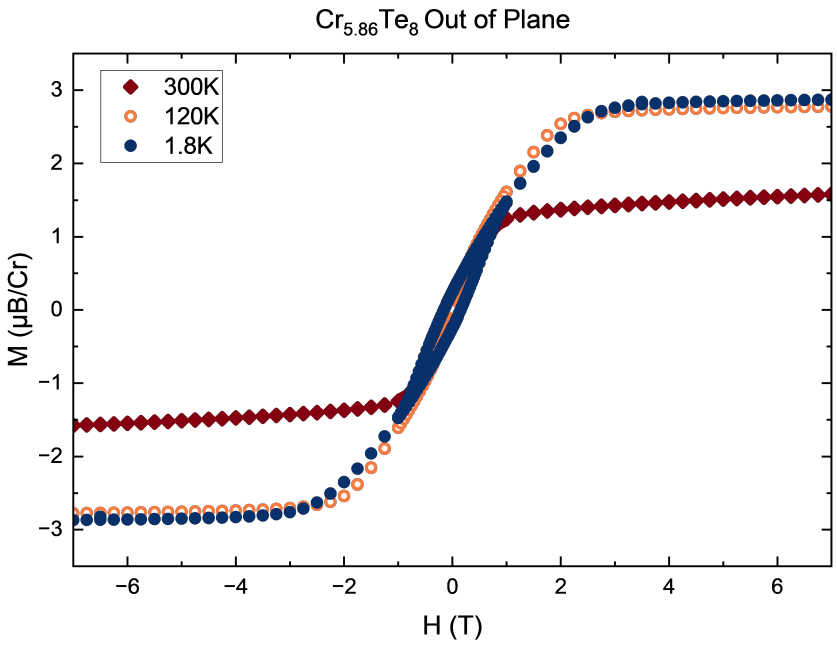

Figure 4.8: Simple soft ferromagnetic ordering is observed in monoclinic $Cr_{5.86}Te_8$ via the field sweep measurements. Some hysteresis is observed at the 2 K temperature scan. The observation of a hysteresis loop beginning at 2 K may be due to ferrimagnetic ordering at low temperature but follow on neutron studies should be preformed to elucidate this possibility.

magnetic susceptibility at 275 K followed by a sharp drop in saturation leading to another complex magnetic phase diagram. Similar observations are seen in Cr_5Te_8 single crystal by Mondal et al. [20] The sharp peak in the in-plane measurements is more characteristic of an anti-ferromagnet and is likely due to the canting of spins which is again observed in the higher chromium content Cr_7Te_8. Field sweep measurements pictured in Figure 4.10 again show opposite magnetization versus field in in-plane measurements and is repeatable but unreported in current literature. Susceptibility in the out of plane measurements of the trigonal sample shows higher susceptibility saturation in the out of plane sample leading us to believe the easy-axis of magnetization is in the *c*-direction of the trigonal samples. Figure 4.11 also shows simple ferromagnetic behavior in the out of plane measurements with a Curie temperature around 300 K. Extrapolating from the solved magnetic structure

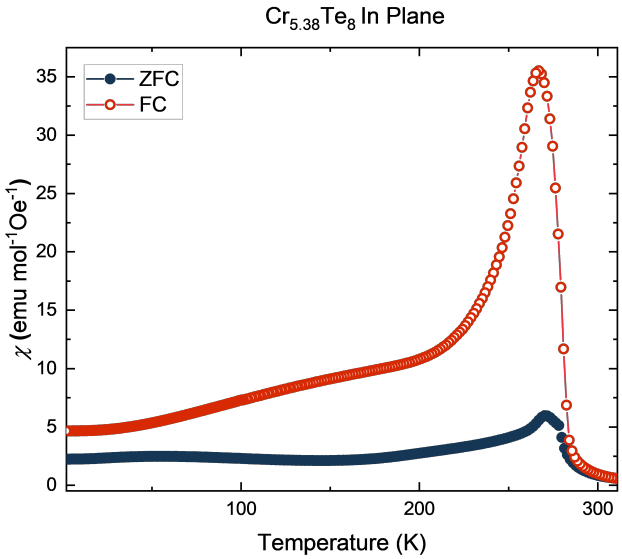

Figure 4.9: Trigonal $Cr_{5.38}Te_8$ is one of the few single crystal samples without observed room temperature ferromagnetism. A sharp increase in magnetic susceptibility followed by a drop in saturation is observed in the in-plane measurements.

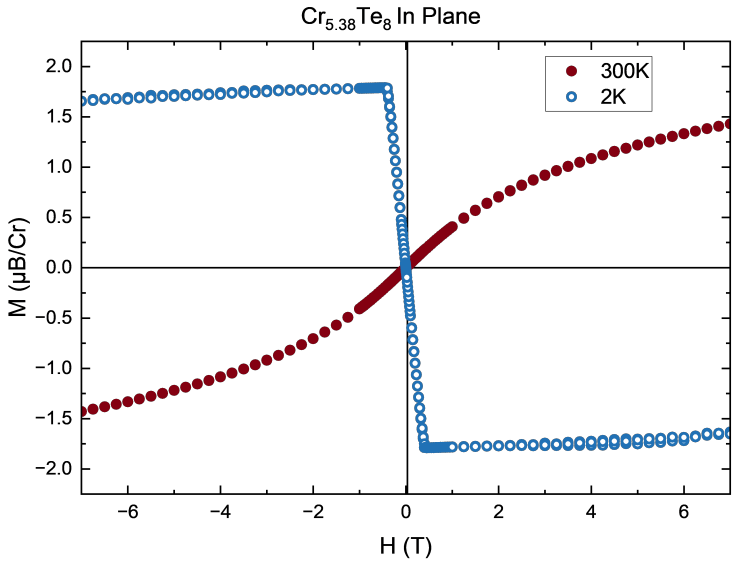

Figure 4.10: Trigonal $Cr_{5.38}Te_8$ exhibits opposite magnetization versus field at low temperatures.

of the hexagonal phase polycrystalline sample this is inline with a majority of the magnetic moments aligning in the out of plane direction with some canting in the *ab* plane. The ad-

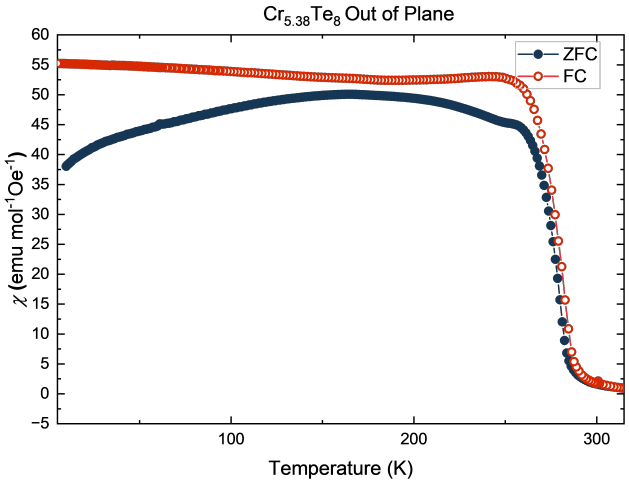

Figure 4.11: Trigonal $Cr_{5.38}Te_8$ shows simple ferromagnetism out of plane with higher susceptibility out of plane indicating the easy axis of magnetization is out of plane.

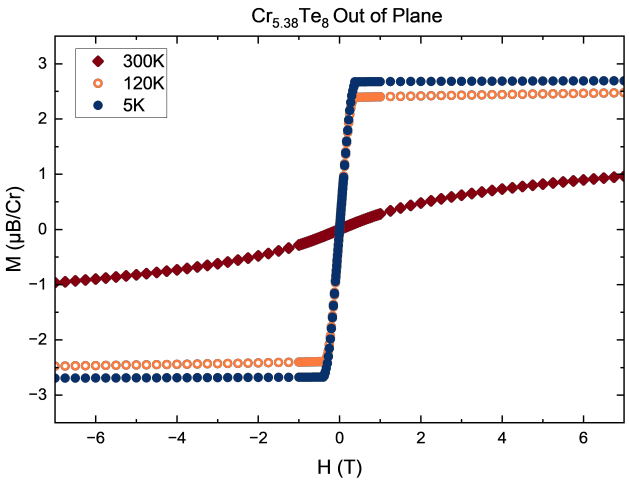

Figure 4.12: Trigonal $Cr_{5.38}Te_8$ shows subdued magnetism at 300K due to the paramagnetic transition being around 270K. Regular soft ferromagnetism is observed at 120K and 2K.

dition of an anti-ferromagnetic moment in the a plane could be the reason a large growth in saturation is observed at 266 K and quickly drops off when cooling to lower temperatures.

In high symmetry hexagonal $Cr_{6.66}Te_8$ single crystals simple ferromagnetic ordering is observed in the in-plane susceptibility measurements. Similar simple ferromagnetic order-

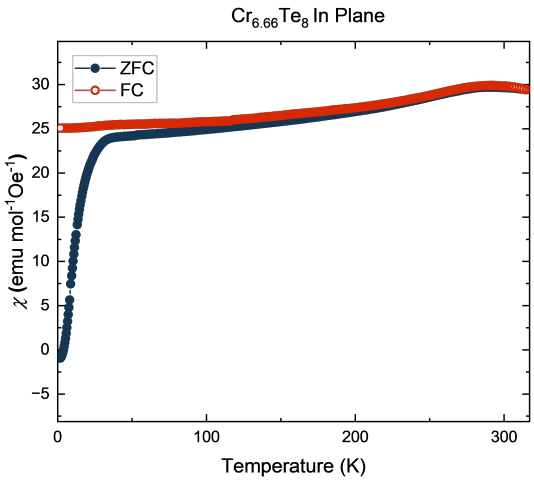

Figure 4.13: Hexagonal $Cr_{6.66}Te_8$ exhibits simple ferromagnetic susceptibility curves.

ing is observed in Purwar et al's work with high symmetry $P63/mmc$ single crystals grown via chemical vapor transport.[71] Easy axis of magnetization is observed parallel the *c*-axis due to high susceptibility in the out of plane measurements. Out of plane magnetic susceptibility measurements also show an easy axis of magnetization parallel to the *c*-axis.[71] Interestingly much sharper slopes are observed in in-plane field sweep measurements which would normal lead to the easy axis of magnetization being in-plane. However our susceptibility data suggests the opposite of this with much higher saturation values recorded in out of plane susceptibility data. No observable hysteresis can be seen implying relatively soft switching of magnetic moments with applied fields. Out of plane measurements show similarly high paramagnetic to ferromagnetic transitions that can not be observed due to the temperature regime at which the SQUID can operate. The observation of some interesting paramagnetic transitions around 70 K are observed that are not observed in the in-plane measurements likely due to the canting of the moments in the *ab* plane.

Out of plane susceptibility measurements of the hexagonal $Cr_{6.66}Te_8$ show a paramagnetic to ferromagnetic transition above 315 K. A meta-magnetic transition is observed

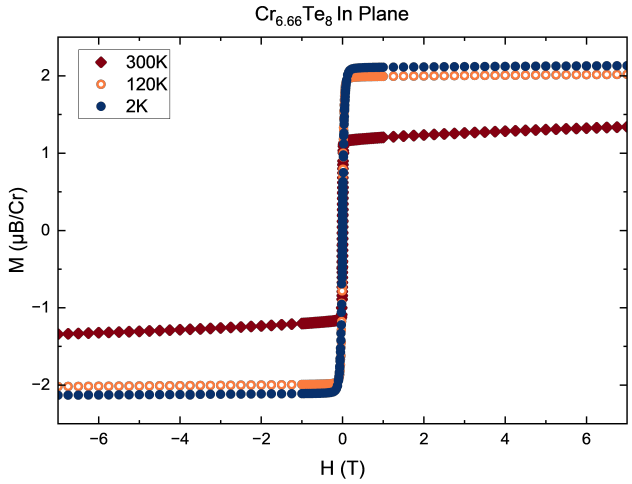

Figure 4.14: Hexagonal $Cr_{6.66}Te_8$ exhibits simple ferromagnetism in field sweep measurements with increasing magnetism with decreased temperature. Field sweeps were preformed at 2 K, 120 K, and 300 K.

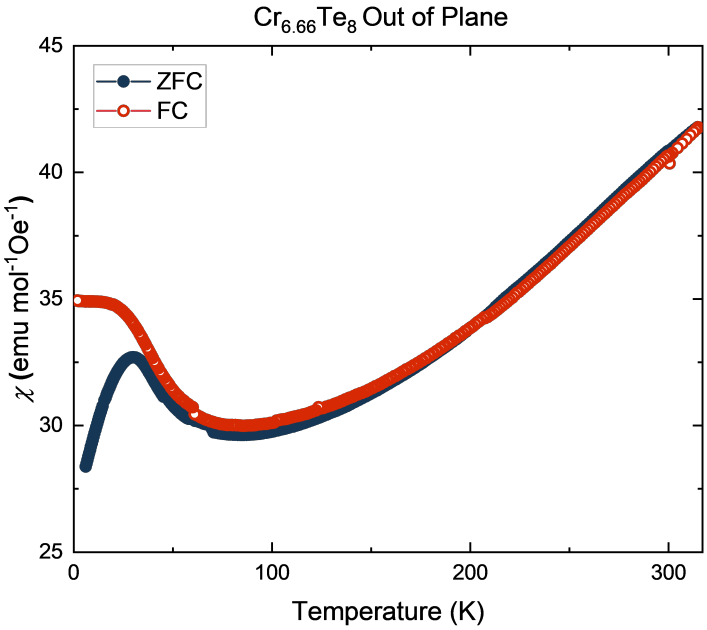

Figure 4.15: Hexagonal $Cr_{6.66}Te_8$ exhibits above room temperature ferromagnetism with a metamagnetic transition around 70 K. Similar features have been observed in the polycrystalline Cr_7Te_8 and the monoclinic $Cr_{5.86}Te_8$.

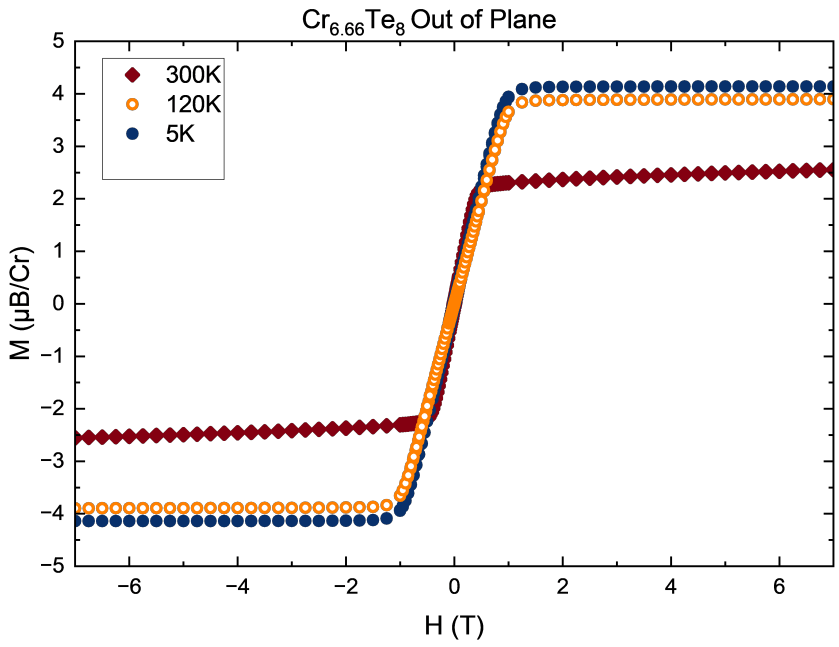

Figure 4.16: Hexagonal $Cr_{6.66}Te_8$ MvH measurements show moment saturation with 1T.

around 70 K as is typically seen in the chromium-telluride family but this time an increase in magnetic moment is observed and is likely contributed to a change in easy axis of the magnetic moments as observed in the polycrystalline sample. Due to the sample being below the Curie temperature pronounced ferromagnetism is observed in the MvH data at 300 K and field sweeps at higher temperature would be needed to show the subdued magnetism of the paramagnetic state. Slightly higher than expected magnetic saturation values are observed in the out of plane $Cr_{6.66}Te_8$ sample and can likely be attributed to the orbital contribution to the magnetic state. The theoretical saturation point was calculated to $M = 3.6\mu_B$. However, calculations were done utilizing Chromium in its 3+ state with three unpaired electrons and no contribution from the orbitals was accounted for. The $Cr_{6.66}Te_8$ hexagonal sample also has some tellurium vacancies as mentioned in Section 4.2 which could contribute to a change in magnetic saturation of the single crystal sample. A stark difference in magnetic saturation can also be observed between the in-plane and out of

plane measurements with higher susceptibility in the out of plane measurements leading us to believe the easy axis is parallel to the *c*-axis. The sudden drop in susceptibility observed in the out of plane measurements again is likely contributed to the change in magnetic easy axis of the samples as seen in the polycrystalline sample and observed in other single crystal samples, mainly the Cr_5Te_8 samples discussed in section 1.4. Pinning of magnetic domains in the c-axis can eventually be overcome when thermal energies are sufficient and a flip in axis is observed in the *ab*-plane.[22]

All of the single crystals grown in section 4.3 show unique magnetic transitions with a common meta-magnetic transition often recorded around 70 K. Increasing chromium content in the self intercalated layers monotonically increases curie temperature independent of crystal structure. Tellurium vacancies may have some impact on the magnetic structure due to the importance of the Cr3d-Te5p covalencey but the affects can not be explained in the scope of this thesis. Continued studies of the chromium telluride family of compounds should be preformed starting with neutron diffraction measurements to determine the magnetic structure of the single crystals. Differences in magnetic easy axis can be compared easily utilizing neutron single crystal diffraction techniques and exact moment canting can be deciphered for samples with non degenerate axis.

4.4 Comparison of Single Crystals

Increasing chromium content across single crystals causes formation of chromium full and chromium deficient layers that stack alternatively as shown in section 4.2. Macro magnetic property measurement has shown that increasing chromium content raises the paramagnetic to ferromagnetic transition temperature. Trigonal $Cr_{5.38}Te_8$ shows below room temperature ferromagnetism with much greater spin canting contributions than is observed in monoclinic $Cr_{5.86}Te_8$ single crystals. When compared to Zhang et al's work a significant increase in Curie temperature is observed in our trigonal single crystal sample with our T_c being roughly 280 K right about the expected value with a monotonic increase in Curie temperature with increasing chromium content. Again similarly to Zhang et al's work a suppression of the anti-ferromagnetic contributions is observed in our single crystal sample with almost no AFM-like contribution around 70 K.[7] A unique feature of the Trigonal $Cr_{5.38}Te_8$ is the stark difference in in and out of plane susceptibility measurements. In-plane measurements show an almost vertical drop in magnetic susceptibility that can be compared to the observed spin flip in the trigonal $Cr_{5+x}Te_8$ where X=-0.1. Zhang et al contribute this to a spin flip from the *ab*-plane to the *c*-axis and is corroborated by other evidence of chromium tellurides experiencing temperature dependent anisotropy.[7] Extrapolating to the Cr_7Te_8 magnetic structures solved via BT-1 neutron diffraction in Chapter 3, it seems that most chromium tellurides undergo a spin flip and re-flip with varying temperature. The underlying reason of the spin flip is still unknown and is suitable for more single crystal neutron diffraction studies. A wide variety in magnetic properties is reported in the chromium telluride family, many of which showing spin flip behavior but some favoring simple ferromagnetic behavior.[72] Magnetic susceptibility data on monoclinic and trigonal Cr_5Te_8 by Lukoschus et al shows no interesting magnetic behavior outside of simple ferromagnetic saturation. These results are contrary to what we observe in our monoclinic

$Cr_{5.86}Te_8$ and trigonal $Cr_{5.38}Te_8$. We observe a meta-magnetic transition in the monoclinic sample below T_c around 70 K which is likely the AFM-canting in the *ab* plane similar to our polycrystalline sample. Again, no difference in susceptibility between in and out of plane measurements was reported by Lukoschus et al. Zhang et al predicted that increased chromium content reduces AFM contributions and is shown in their work but work across groups shows a different story. Low chromium content Cr_5Te_8 in Lukoshus group shows no AFM-like contributions while Zhang et al only begins to see normal ferromagnetic order in the high chromium content regime.

Neutron diffraction studies of the monoclinic phase Cr_5Te_8 in polycrystalline form show AFM-like contributions as observed in the polycrystalline Cr_7Te_8 samples.[21] However, Huang et al utilized the unconventional $F2/m$ space group to fit the neutron diffraction data. When attempting to fit our polycrystalline monoclinic Cr_7Te_8 X-ray diffraction data utilizing the $F2/m$ space group a rather poor refinement resulted. This raises concerns over our monoclinic crystals and Huang et al's single crystals having the same symmetry elements. Due to this limited comparisons can be drawn from the neutron experiment preformed and a more complete study of our monoclinic chromium telluride single crystals should be preformed to flesh out the possibility of spin flipping and re-flipping. It os also worth noting that our observed Curie temperature is roughly 90 K higher than what is observed by Huang et al's group in neutron diffraction.[21] This is likely due to the increased chromium content in our monoclinic crystals as shown in Zhang et al's tunability study.[7]

Above room temperature transitions are recorded in the monoclinic system with more regular ferromagnetic contributions. AFM-like metamagnetic transitions are still observed at around 70 K similar to what is seen in the chromium rich Cr_7Te_8 polycrystalline samples taken for neutron diffraction. Hexagonal phase $Cr_6.66Te_8$ shows the same chromium deficient and chromium full stacking layers but also experiences tellurium vacancies due to the quenching process utilized to lock in a high symmetry space group in the crystal

lattice. Tellurium vacancies seem to have limited contributions in altering the magnetic properties of the Chromium-Telluride system. Ferromagnetic ordering is still observed in the hexagonal phase with no-meta magnetic transitions observed via MPMS measurements. The interactions of the Cr 3_d and Te 5_p orbitals must contribute to some of the AFM-like spin canting observed in the Cr_7Te_8 polycrystalline sample. Single crystal analysis should be preformed on the hexagonal phase single crystal so that tellurium vacancies impact on the magnetic structure can be explored and contrasted with just chromium vacancies. DFT suggests that both orbital interactions are important in the itinerant magnetic system but no studies have been preformed to decipher which interaction causes more of the spin-canting behavior observed in the single crystal and polycrystalline samples.[19]

Chapter 5: Conclusions and Open Problems

Polycrystalline Cr_7Te_8 in both meta-stable hexagonal phase and annealed monoclinic phase were synthesized and macro and micro magnetic properties were measured utilizing neutron diffraction and MPMS magnetometer. Meta-stable hexagonal phase Cr_7Te_8 undergoes two meta-magnetic transitions with a change in magnetic easy axis to in plane at 150 K and a realignment to the c-axis at 5 K. AFM-like contributions are encountered below 298 K where some spin canting begins to be observed and a level of AFM-like contributions to the magnetic moment are observed. Attempts at growing single crystals of Cr_7Te_8 should be continued so that the exact magnetic structure of the hexagonal Cr_7Te_8 can be studied. Comparisons with the easily grown monoclinic phase could help aid in the understanding of chromium disorders affect on the magnetic structure.

Single crystal samples were then synthesized utilizing chemical vapor transport techniques in an attempt to grow the meta-stable hexagonal phase Cr_7Te_8. A plethora of single crystal samples were grown to include trigonal Cr_5Te_8, monoclinic Cr_5Te_8, and hexagonal $Cr_{1-x}Te$ where X= .17. Macro magnetic properties were measured utilizing a SQUID magnetometer and interesting macro magnetic transitions were observed that should be studied utilizing single crystal neutron diffraction. Contributions of tellurium vacancies in the hexagonal $Cr_{6.66}Te_8$ should be studied and compared to the polycrystalline magnetic structures solved via BT-1 neutron diffraction.

A study observing increasing chromium contents affect on the magnetic structure of the chromium-telluride family should also be preformed to see when a spin-cant behavior

begins to be observed. Elucidating the reason behind antiferromagnetic contributions in the crystal lattice may lead to chromium tellurides having increased use in 2D/3D hetero-structure device fabrication. When the phase-diagram reaches the chromium rich side of the chart, paramagnetic to ferromagnetic transition temperature is raised to above room temperature lending to the chromium-telluride pseudo van der Waals materials being of particular use in hetero-structure device fabrication. Studies have shown that increasing chromium content often reduces the AFM moment and the ferromagnetic moment begins to dominate. However, polycrystalline studies of the chromium rich Cr_7Te_8 have shown this is not always the case. Single crystal neutron studies of the hexagonal phase Cr_7Te_8 should be preformed to show the impact of chromium vacancies on AFM contributions to the atomic scale magnetic structure. Future studies should also be preformed on the impact of distortions of the chromium telluride octahedron. Changes in closest neighbor Cr-Cr distances seem to have a large impact on the magnetic structure of the chromium telluride family. Doping of chromium telluride with varying amounts of selenium may be interesting to see when the compound becomes an anti-ferromagnet and neutron studies may be able to determine why this is the case when observing contractions in th c-axis.

Bibliography

[1] C. Biz, J. Gracia, and M. Fianchini, "Review on magnetism in catalysis: From theory to pemfc applications of 3d metal pt-based alloys," *International Journal of Molecular Sciences*, vol. 23, no. 23, p. 14768, 2022.

[2] Y. Wen, Z. Liu, Y. Zhang, C. Xia, B. Zhai, X. Zhang, G. Zhai, C. Shen, P. He, R. Cheng, *et al.*, "Tunable room-temperature ferromagnetism in two-dimensional cr2te3," *Nano letters*, vol. 20, no. 5, pp. 3130–3139, 2020.

[3] A. K. Geim and K. S. Novoselov, "The rise of graphene," *Nature materials*, vol. 6, no. 3, pp. 183–191, 2007.

[4] Z. Fei, B. Huang, P. Malinowski, W. Wang, T. Song, J. Sanchez, W. Yao, D. Xiao, X. Zhu, A. F. May, *et al.*, "Two-dimensional itinerant ferromagnetism in atomically thin fe3gete2," *Nature materials*, vol. 17, no. 9, pp. 778–782, 2018.

[5] A. Goldman, *Handbook of modern ferromagnetic materials*, vol. 505. Springer Science & Business Media, 2012.

[6] A. Goswami, N. Ng, E. Yakubu, A. M. Abeykoon, and S. Guchhait, "Critical behavior in monoclinic cr 3 te 4," *Physical Review B*, vol. 109, no. 5, p. 054413, 2024.

[7] L.-Z. Zhang, X.-D. He, A.-L. Zhang, Q.-L. Xiao, W.-L. Lu, F. Chen, Z. Feng, S. Cao, J. Zhang, and J.-Y. Ge, "Tunable curie temperature in layered ferromagnetic cr5+ xte8 single crystals," *APL Materials*, vol. 8, no. 3, 2020.

[8] K. S. Novoselov, A. Mishchenko, A. Carvalho, and A. Castro Neto, "2d materials and van der waals heterostructures," *Science*, vol. 353, no. 6298, p. aac9439, 2016.

[9] H. C. Mandujano, G. S. Salas, T. Li, P. Y. Zavalij, A. Manjón-Sanz, N. P. Butch, and E. E. Rodriguez, "Itinerant *a*-type antiferromagnetic order in $co_{1/4}tase_2$," *Phys. Rev. B*, vol. 110, p. 144420, Oct 2024.

[10] Y. Deng, Y. Yu, Y. Song, J. Zhang, N. Z. Wang, Z. Sun, Y. Yi, Y. Z. Wu, S. Wu, J. Zhu, *et al.*, "Gate-tunable room-temperature ferromagnetism in two-dimensional fe3gete2," *Nature*, vol. 563, no. 7729, pp. 94–99, 2018.

[11] C. Gong, L. Li, Z. Li, H. Ji, A. Stern, Y. Xia, T. Cao, W. Bao, C. Wang, Y. Wang, *et al.*, "Discovery of intrinsic ferromagnetism in two-dimensional van der waals crystals," *Nature*, vol. 546, no. 7657, pp. 265–269, 2017.

[12] C. Gong, G. Lee, B. Shan, E. M. Vogel, R. M. Wallace, and K. Cho, "First-principles study of metal–graphene interfaces," *Journal of Applied Physics*, vol. 108, p. 123711, 12 2010.

[13] B. Xin, K. Zou, D. Liu, S. Liang, H. Dong, F. Lu, C. Gong, F. Luo, and W.-H. Wang, "First-principles studies of the mixed-dimensional van der waals heterostructures of graphene/mnf4," *Journal of Applied Physics*, vol. 132, no. 8, 2022.

[14] A. Wang, A. Rahman, Z. Du, W. Liu, J. Li, J. Fan, C. Ma, M. Ge, L. Pi, Y. Zhang, *et al.*, "Temperature-dependent anisotropy variation in quasi-two-dimensional ferromagnetic cr5te8," *Applied Physics Letters*, vol. 124, no. 17, 2024.

[15] R. Yao, Z. Liu, Y. Ma, L. Xu, Y. He, W. Ai, Y. Li, F. Lu, H. Dong, Z. Gao, *et al.*, "Controlled synthesis of 2d ferromagnetic/antiferromagnetic cr7te8/mnte vertical heterostructures for high-tunable coercivity," *ACS nano*, vol. 18, no. 34, pp. 23508–23517, 2024.

[16] K. Meng, Z. Li, Y. Shen, X. Bi, J. Rao, Y. Qian, Z. Gao, P. Chen, C. Qiu, F. Qin, *et al.*, "Gate tunable labyrinth domain structures in a van der waals itinerant ferromagnet cr7te8," *Chinese Physics Letters*, vol. 41, no. 9, p. 097501, 2024.

[17] J. Liu, B. Ding, J. Liang, X. Li, Y. Yao, and W. Wang, "Magnetic skyrmionic bubbles at room temperature and sign reversal of the topological hall effect in a layered ferromagnet cr0. 87te," *ACS nano*, vol. 16, no. 9, pp. 13911–13918, 2022.

[18] C. Gong and X. Zhang, "Two-dimensional magnetic crystals and emergent heterostructure devices," *Science*, vol. 363, no. 6428, p. eaav4450, 2019.

[19] J. Dijkstra, H. Weitering, C. Van Bruggen, C. Haas, and R. De Groot, "Band-structure calculations, and magnetic and transport properties of ferromagnetic chromium tellurides (crte, cr3te4, cr2te3)," *Journal of Physics: Condensed Matter*, vol. 1, no. 46, p. 9141, 1989.

[20] R. Mondal, R. Kulkarni, and A. Thamizhavel, "Anisotropic magnetic properties and critical behaviour studies of trigonal cr5te8 single crystal," *Journal of Magnetism and Magnetic Materials*, vol. 483, pp. 27–33, 2019.

[21] Z.-L. Huang, W. Kockelmann, M. Telling, and W. Bensch, "A neutron diffraction study of structural and magnetic properties of monoclinic cr5te8," *Solid state sciences*, vol. 10, no. 8, pp. 1099–1105, 2008.

[22] X.-H. Luo, W.-J. Ren, and Z.-D. Zhang, "Magnetic properties and magnetocaloric effect of a trigonal te-rich cr5te8 single crystal," *Journal of Magnetism and Magnetic Materials*, vol. 445, pp. 37–43, 2018.

[23] D. C. Freitas, R. Weht, A. Sulpice, G. Remenyi, P. Strobel, F. Gay, J. Marcus, and M. Núñez-Regueiro, "Ferromagnetism in layered metastable 1t-crte2," *Journal of Physics: Condensed Matter*, vol. 27, no. 17, p. 176002, 2015.

[24] Z.-L. Huang, W. Bensch, D. Benea, and H. Ebert, "Crystal structures, unusual magnetic properties and electronic band structures of cr5- xtixte8," *Journal of Solid State Chemistry*, vol. 178, no. 9, pp. 2778–2790, 2005.

[25] T. Hashimoto and M. Yamaguchi, "Magnetic properties of cr7te8," *Journal of the Physical Society of Japan*, vol. 27, no. 5, pp. 1121–1126, 1969.

[26] Y. Ma, R. Yao, J. Wu, Z. Gao, and F. Luo, "Unusual anomalous hall effect in two-dimensional ferromagnetic cr7te8," *Molecules*, vol. 29, no. 21, p. 5068, 2024.

[27] J. Wontcheu, W. Bensch, S. Mankovsky, S. Polesya, H. Ebert, R. K. Kremer, and E. Brücher, "Anion substitution effects on the structure and magnetism of the chromium chalcogenide cr5te8—part iii: Structures and magnetism of the high-temperature modification cr (1+ x) q2 and the low-temperature modification cr (5+ x) q8 (q= te, se; te: Se= 5: 3)," *Journal of Solid State Chemistry*, vol. 181, no. 6, pp. 1492–1505, 2008.

[28] J. R. Chamorro and T. M. McQueen, "Progress toward solid state synthesis by design," *Accounts of chemical research*, vol. 51, no. 11, pp. 2918–2925, 2018.

[29] M. Jansen, "A concept for synthesis planning in solid-state chemistry," *Angewandte Chemie International Edition*, vol. 41, no. 20, pp. 3746–3766, 2002.

[30] D. Wang, F. Luo, M. Lu, X. Xie, L. Huang, and W. Huang, "Chemical vapor transport reactions for synthesizing layered materials and their 2d counterparts," *Small*, vol. 15, no. 40, p. 1804404, 2019.

[31] W. L. Bragg, "The specular reflection of x-rays.," *Nature*, vol. 90, no. 2250, pp. 410–410, 1912.

[32] A. A. Bunaciu, E. G. UdriŞTioiu, and H. Y. Aboul-Enein, "X-ray diffraction: instrumentation and applications," *Critical reviews in analytical chemistry*, vol. 45, no. 4, pp. 289–299, 2015.

[33] N. Iwashita, "X-ray powder diffraction," in *Materials science and engineering of carbon*, pp. 7–25, Elsevier, 2016.

[34] R. Reynolds, "Principles of powder diffraction," *Modern powder diffraction*, vol. 20, pp. 1–17, 1989.

[35] M. Ladd and R. Palmer, "I x-rays, x-ray diffraction, and structure factors: Ii intensities and intensity statistics," in *Structure Determination by X-ray Crystallography*, pp. 117–211, Springer, 2003.

[36] Z. Ren, D. Bourgeois, J. R. Helliwell, K. Moffat, V. Srajer, and B. L. Stoddard, "Laue crystallography: coming of age," *Journal of Synchrotron Radiation*, vol. 6, no. 4, pp. 891–917, 1999.

[37] A. Arnaud, W. Guediche, C. Remacha, E. Roméro, and H. Proudhon, "A laboratory transmission diffraction laue setup to evaluate single-crystal quality," *Journal of Applied Crystallography*, vol. 53, no. 4, pp. 914–926, 2020.

[38] J. Hastings, W. Thomlinson, and D. Cox, "Synchrotron x-ray powder diffraction," *Journal of applied crystallography*, vol. 17, no. 2, pp. 85–95, 1984.

[39] O. H. Seeck and B. Murphy, *X-ray diffraction: modern experimental techniques*. CRC Press, 2015.

[40] G. Rosenbaum, K. C. Holmes, and J. Witz, "Synchrotron radiation as a source for x-ray diffraction," *Nature*, vol. 230, no. 5294, pp. 434–437, 1971.

[41] K. Wille, "Synchrotron radiation sources," *Reports on Progress in Physics*, vol. 54, no. 8, p. 1005, 1991.

[42] L. McCusker, R. Von Dreele, D. Cox, D. Louër, and P. Scardi, "Rietveld refinement guidelines," *Journal of Applied Crystallography*, vol. 32, no. 1, pp. 36–50, 1999.

[43] B. Toby, "Rietveld refinement," 2019.

[44] J. E. Post and D. L. Bish, "Rietveld refinement of crystal structures using powder x-ray diffraction data," *Modern powder diffraction*, vol. 20, pp. 277–308, 1989.

[45] R. Von Dreele, "Rietveld refinement," 2008.

[46] D. Cialla-May, M. Schmitt, and J. Popp, "Theoretical principles of raman spectroscopy," *Physical Sciences Reviews*, vol. 4, no. 6, 2019.

[47] P. Larkin, *Infrared and Raman spectroscopy: principles and spectral interpretation*. Elsevier, 2017.

[48] V.-D. Hodoroaba, "Energy-dispersive x-ray spectroscopy (eds)," in *Characterization of Nanoparticles*, pp. 397–417, Elsevier, 2020.

[49] D. Shindo, T. Oikawa, D. Shindo, and T. Oikawa, "Energy dispersive x-ray spectroscopy," *Analytical electron microscopy for materials science*, pp. 81–102, 2002.

[50] R. E. Dinnebier and S. J. Billinge, *Powder diffraction: theory and practice*. Royal society of chemistry, 2015.

[51] E. Ressouche, "Reminder: Magnetic structures description and determination by neutron diffraction," *École thématique de la Société Française de la Neutronique*, vol. 13, p. 02001, 2014.

[52] A. Albinati and B. Willis, "The rietveld method in neutron and x-ray powder diffraction," *Journal of Applied Crystallography*, vol. 15, no. 4, pp. 361–374, 1982.

[53] T. Saerbeck, "Magnetic exchange phenomena probed by neutron scattering," *Solid State Physics*, vol. 65, pp. 237–352, 2014.

[54] S. Yusuf and A. Kumar, "Neutron scattering of advanced magnetic materials," *Applied Physics Reviews*, vol. 4, no. 3, 2017.

[55] S. V. Gallego, J. M. Perez-Mato, L. Elcoro, E. S. Tasci, R. M. Hanson, M. I. Aroyo, and G. Madariaga, "Magndata: towards a database of magnetic structures. ii. the incommensurate case," *Journal of Applied Crystallography*, vol. 49, no. 6, pp. 1941–1956, 2016.

[56] National Institute of Standards and Technology (NIST), "High resolution powder diffractometer - bt-1," n.d. Accessed: 2024-12-11.

[57] A. Wills, "Magnetic structures and their determination using group theory," *Le Journal de Physique IV*, vol. 11, no. PR9, pp. Pr9–133, 2001.

[58] S. Mugiraneza and A. M. Hallas, "Tutorial: a beginner's guide to interpreting magnetic susceptibility data with the curie-weiss law," *Communications Physics*, vol. 5, no. 1, p. 95, 2022.

[59] S. R. Power and M. S. Ferreira, "Indirect exchange and ruderman–kittel–kasuya–yosida (rkky) interactions in magnetically-doped graphene," *Crystals*, vol. 3, no. 1, pp. 49–78, 2013.

[60] S. Foner, "Versatile and sensitive vibrating-sample magnetometer," *Review of Scientific Instruments*, vol. 30, no. 7, pp. 548–557, 1959.

[61] S. A. H. Shah, "Vibrating sample magnetometery: analysis and construction," *Syed Babar Ali School of Science and Engineering, LUMS*, 2013.

[62] R. Kleiner, D. Koelle, F. Ludwig, and J. Clarke, "Superconducting quantum interference devices: State of the art and applications," *Proceedings of the IEEE*, vol. 92, no. 10, pp. 1534–1548, 2004.

[63] A. Aharoni, *Introduction to the Theory of Ferromagnetism*, vol. 109. Clarendon Press, 2000.

[64] L. Fritsche and B. Weimert, "First-principles theory of ferromagnetic and antiferromagnetic order," *physica status solidi (b)*, vol. 208, no. 2, pp. 287–337, 1998.

[65] B. Chen, X. Wu, Z. Liao, Z. Fu, B. Xu, M. Wang, and B. Shen, "Sign-reversal anomalous hall effect driven by a magnetic transition in cr _{7-\delta} *te* _8," *arXivpreprintarXiv* : 2404.00659, 2024.

[66] A. Ohsawa, Y. Yamaguchi, N. Kazama, H. Yamauchi, and H. Watanabe, "Magnetic anisotropy of cr1-x te with x= 0.077," *Journal of the Physical Society of Japan*, vol. 33, no. 5, pp. 1303–1307, 1972.

[67] H. Lv, W. Lu, D. Shao, Y. Liu, and Y. Sun, "Strain-controlled switch between ferromagnetism and antiferromagnetism in 1 t-cr x 2 (x= se, te) monolayers," *Physical Review B*, vol. 92, no. 21, p. 214419, 2015.

[68] C. Conner, A. Sarikhani, T. Volz, M. Vaninger, X. He, S. Kelley, J. Cook, A. Sah, J. Clark, H. Lucker, *et al.*, "Enhanced antiferromagnetic phase in metastable self-intercalated cr _{1+x} te _2 compounds," *arXiv preprint arXiv:2411.13721*, 2024.

[69] G. Chattopadhyay, "The cr-te (chromium-tellurium) system," *Journal of phase equilibria*, vol. 15, pp. 431–440, 1994.

[70] Z. Jiang, X. Luo, J. Yan, J. Gao, W. Wang, G. Zhao, Y. Sun, J. Si, W. Lu, P. Tong, *et al.*, "Magnetic anisotropy and anomalous hall effect in monoclinic single crystal cr 5 te 8," *Physical Review B*, vol. 102, no. 14, p. 144433, 2020.

[71] S. Purwar, S. Changdar, S. Ghosh, T. K. Bhowmik, and S. Thirupathaiah, "Intricate magnetism and topological hall effect observed in cr _{0.83} te," *arXiv preprint arXiv:2404.07237*, 2024.

[72] K. Lukoschus, S. Kraschinski, C. Näther, W. Bensch, and R. Kremer, "Magnetic properties and low temperature x-ray studies of the weak ferromagnetic monoclinic and trigonal chromium tellurides cr5te8," *Journal of Solid State Chemistry*, vol. 177, no. 3, pp. 951–959, 2004.